J. Fluid Mech. (2011), *vol.* 688, *pp.* 390–421.
doi:10.1017/jfm.2011.381

Viscous irrotational analysis of the deformation and break-up time of a bubble or drop in uniaxial straining flow

J. C. Padrino[1]† and D. D. Joseph[1,2]

[1] Department of Aerospace Engineering and Mechanics, University of Minnesota, Minneapolis, MN 55455, USA

[2] Department of Mechanical and Aerospace Engineering, University of California–Irvine, Irvine, CA 92697, USA

(Received 5 April 2010; revised 11 May 2011; accepted 8 September 2011; first published online 9 November 2011)

The nonlinear deformation and break-up of a bubble or drop immersed in a uniaxial extensional flow of an incompressible viscous fluid is analysed by means of viscous potential flow. In this approximation, the flow field is irrotational and viscosity enters through the balance of normal stresses at the interface. The governing equations are solved numerically to track the motion of the interface by coupling a boundary-element method with a time-integration routine. When break-up occurs, the break-up time computed here is compared with results obtained elsewhere from numerical simulations of the Navier–Stokes equations (Revuelta, Rodríguez-Rodríguez & Martínez-Bazán *J. Fluid Mech.*, vol. 551, 2006, p. 175), which thus keeps vorticity in the analysis, for several combinations of the relevant dimensionless parameters of the problem. For the bubble, for Weber numbers $3 \leqslant We \leqslant 6$, predictions from viscous potential flow shows good agreement with the results from the Navier–Stokes equations for the bubble break-up time, whereas for larger We, the former underpredicts the results given by the latter. When viscosity is included, larger break-up times are predicted with respect to the inviscid case for the same We. For the drop, and considering moderate Reynolds numbers, Re, increasing the viscous effects of the irrotational motion produces large, elongated drops that take longer to break up in comparison with results for inviscid fluids. For larger Re, it comes as a surprise that break-up times smaller than the inviscid limit are obtained. Unfortunately, results from numerical analyses of the incompressible, unsteady Navier–Stokes equations for the case of a drop have not been presented in the literature, to the best of the authors' knowledge; hence, comparison with the viscous irrotational analysis is not possible.

Key words: breakup/coalescence, bubble dynamics, drops

1. Introduction

The break-up of bubbles and drops by a turbulent immiscible flow plays a key role in transfer phenomena occurring in engineering applications and natural settings.

† Email address for correspondence: padr0006@umn.edu
This paper is dedicated to the memory of Daniel D. Joseph (1929–2011).

The rate of mass, heat and momentum transfer between a dispersed phase and a continuous phase strongly depends on the existing contact or interfacial area, which in turn is determined by the deformation and break-up of the fluid particles. For instance, this is of paramount importance for the performance of gas–liquid and liquid–liquid chemical reactors and separators. Also, the exchange of carbon dioxide, water vapour and other species between the oceans and the atmosphere, which has large-scale environmental implications, is known to be associated with the bubble size distribution resulting from interaction of the turbulence within the bulk of the water with the air entrained by the dynamics of sea waves (Melville 1996; Martínez-Bazán, Montanes & Lasheras 1999*a*,*b*, and references therein). Therefore, an understanding of the mechanism of turbulent break-up of bubbles or drops has been central to developing predictive models applicable to these and many other processes. In particular, the particle break-up time is an essential parameter in the description of these phenomena.

After the pioneering works of Kolmogorov (1949) and later of Hinze (1955), it has been established that turbulent break-up of a fluid particle results as a consequence of the overcoming of the shape-preserving surface tension forces by the pressure fluctuations acting on the particle. Moreover, it has been ascertained that characterizing the local turbulent fluid dynamics prevailing around the bubble or drop suffices to describe the changes in its morphology. Another break-up mechanism, first described by Risso & Fabre (1998) and known as subcritical break-up, in opposition to the supercritical mechanism just presented, consists of the occurrence of bubble resonance with a series of consecutive, subcritical (i.e. moderate) turbulent eddies that lead to large oscillations and eventual break-up of the bubble.

After examining available experimental data on bubble and drop break-up in a turbulent water stream obtained by Eastwood, Armi & Lasheras (2004) and Rodríguez-Rodríguez (2004), respectively, and by performing numerical simulations, Rodríguez-Rodríguez, Gordillo & Martínez-Bazán (2006) (hereinafter RDZ) have convincingly shown that this phenomenon can be modelled, as a first approximation, by considering a bubble or drop, initially spherical, immersed in a uniaxial straining flow of an incompressible fluid, using a reference frame that moves with the mean velocity of the background flow. Although simple, this model retains the most relevant features of the process, thus avoiding expensive three-dimensional numerical computations involving the tracking of deforming interfaces in a turbulent flow characterized by unsteady structures with various length scales. Indeed, the images observed by RDZ revealed that the bubbles or drops follow a 'cigar-shape' elongation leading to break-up that is nearly axisymmetric. Moreover, their observations suggest that a single turbulent eddy is the cause of breakage and 'whose characteristic turnover time is larger than the break-up time', thereby justifying the assumption of a steady flow in the far field (i.e. fluctuations are discarded as the cause of break-up). Indeed, Risso & Fabre (1998) observed in experiments that an initially non-deformed bubble may be deformed and broken by turbulent eddies strong enough to generate abrupt break-up. RDZ further assume that the particle characteristic size falls within the inertial subrange of the turbulent energy spectrum, hence the fluids are considered inviscid. In their simulations, the velocity field is irrotational. The numerical simulations are carried out by RDZ using the boundary element method and the bubble or drop break-up time is predicted as a function of the Weber number, which measures the relative importance of the external flow inertia versus the force due to surface tension, and the internal to external density ratio. Thus, values of the Weber number and density ratio must be entered before running a simulation. To be able to specify a Weber number representative of the characteristics of the turbulent flow, RDZ derived a formula that links the magnitude of the Weber number to the dissipation rate of turbulent kinetic energy per unit mass. Their simulations result in particle break-up when the

actual Weber number is larger than a critical Weber number; otherwise, the bubble or drop oscillates and does not break-up in agreement with experimental evidence. For the case of the bubble, binary break-up is predicted; that is, the bubble breaks up into two equal pieces in accordance with experiments (Martínez-Bazán *et al.* 1999*b*; Rodríguez-Rodríguez, Martínez-Bazán & Montanes 2003; Andersson & Andersson 2006); the computed break-up time also agrees with experimental measurements by Martínez-Bazán *et al.* (1999*a*) and Rodríguez-Rodríguez (2004).

On the other hand, in the case of the drop, the break-up is tertiary (e.g. Andersson & Andersson 2006) as two symmetric daughter drops are formed at both ends of an intermediate ligament that becomes slender, with length larger than the initial drop radius for large Weber numbers, as the internal to external density ratio becomes of order one. For Weber numbers close to the critical value, the central satellite drop is small in volume. In this case, RDZ point out that predictions for the break-up time and critical Weber number do not agree with the experimental measurements. They assert that this discrepancy results because the drop takes the form of a long ligament with a length much larger than the size of the breaking eddy. The elongated drop thus turns around itself as observed in the experiments. Therefore, the approximation of the local fluid motion as an axisymmetric straining motion is no longer valid. Beyond this weakness, those authors state that the simple model is able to qualitatively describe important features of the process as the tertiary break-up and the size of the intermediate ligament.

Revuelta, Rodríguez-Rodríguez & Martínez-Bazán (2006) (hereinafter REV) add a viscous correction to the inviscid break-up time predicted by RDZ by solving the unsteady incompressible Navier–Stokes equations for a bubble immersed in the uniaxial extensional flow of a liquid using a level set method on a fixed mesh. Since viscosity enters the analysis, two additional dimensionless parameters appear in the formulation, namely, the internal to external viscosity ratio and a Reynolds number based upon the liquid properties, the bubble initial radius and the principal strain rate. In terms of this Reynolds number, the correction to the break-up time is found to be $O(Re^{-1})$. They also found that for a fixed Weber number, the smaller the Reynolds number, the longer it takes the bubble to break up. Therefore, the break-up time computed for inviscid fluids, i.e. $Re \to \infty$, determines a lower bound. Moreover, they obtained that for a fixed Reynolds number, the break-up time reaches a plateau as the Weber number increases. They also found that the critical Weber number $We_c = 2.22 \pm 0.005$, which is almost the same as that found by RDZ, is independent of the Reynolds number for $Re \geqslant 20$. In addition, REV also considered a fluctuating principal strain rate in the far field to model the mechanism of resonance of the bubble with passing turbulent structures, a process that has been described above.

A relevant antecedent of the work of REV is the paper by Kang & Leal (1987) on the dynamics of a bubble in a uniaxial extensional flow with a steady strain rate. They focused on finding the maximum critical Weber number for which a steady solution exists by solving the unsteady incompressible Navier–Stokes equations for the external liquid. However, they do not present results on either the break-up time or the bubble morphology in an event of break-up. Kang & Leal (1990) also studied the bubble dynamics when the uniaxial straining motion in the far field is time-periodic. In the case of a drop in a uniaxial extensional flow of another liquid, the literature search revealed, surprisingly, that the numerical solution of the incompressible Navier–Stokes equations has been carried out only by Ramaswamy & Leal (1997), dropping the unsteady term. Therefore, information on the drop break-up time is not provided and their results are concerned with the critical Weber number below which a steady shape exists. The vast majority of the computational work for the transient of this flow

configuration has been conducted neglecting inertia in the limit of Stokes flow as shown, for example, in the review paper by Guido & Greco (2004).

The theories of potential flow of viscous fluids, i.e. viscous potential flow and the dissipation method, which is based upon the mechanical energy equation, have been applied to problems of *linear* stability analysis of diverse origin, as well as to problems of *small* wave dynamics on an interface or free surface (Joseph, Funada & Wang 2007). Results from these analyses have shown that excellent to reasonable agreement can be obtained with exact solutions from the linearized Navier–Stokes equations, which retain the effects of vorticity, or with experimental data. The question of to what extent the viscous irrotational theories, in particular, viscous potential flow, can be used to predict the *nonlinear* motion of an interface is the subject of this investigation.

In this work, the dynamics of the interface of a bubble or drop of an incompressible fluid immersed in another incompressible fluid subjected to a uniaxial extensional flow is studied. The fluids in this system are viscous and the motion is assumed to be irrotational for all time. For the bubble, the internal to external fluid density ratio is set to be very small in comparison with unity and, for the case of the drop, this ratio is of order one. The solution of the governing equations is sought through a numerical method that couples a boundary integral formulation with a time integration scheme following the algorithm proposed by RDZ. In a sense, this is an extension of the work of RDZ for inviscid fluids to include the viscous effects of the irrotational motion via the dynamic balance at the interface that contains the viscous normal stresses. The main objective is the comparison of the interfacial shapes as time advances and the break-up time computed using the viscous irrotational approximation with published results obtained from the solution of the incompressible fully viscous Navier–Stokes equations, which keep the rotational component of the flow field, for the case of the bubble (REV). For the case of the drop, we present numerical results from the viscous potential flow theory; however, we are not able to compare with results from a transient analysis of a flow satisfying the Navier–Stokes equations because, as mentioned above and to the best of the authors' knowledge, no works have been presented in the literature in which these computations have been performed.

This paper is organized as follows. This section is followed by a brief literature review on the boundary element method applied to the problem of interfacial flows for viscous fluids. Next, in § 3, the problem formulation and the numerical method are described in detail. In § 4, the validation of the numerical method (§ 4.1) and the results for the nonlinear deformation of a bubble (§ 4.2) and drop (§ 4.3) with viscous effects are presented and discussed. Finally, concluding remarks are given in § 5.

2. Boundary integral methods for viscous potential flow

In the vast majority of the cases, boundary integral formulations based on the potential theory have been implemented to compute interfacial flows of inviscid, irrotational flows. In only a few cases has this method been applied to analyse the interfacial flow of viscous fluids, the reason being that the effect of vorticity generated at interfaces or solid boundaries cannot be accounted for. A viscous potential flow analysis of the deformation of a rising three-dimensional bubble was presented by Miksis, Vanden-Broeck & Keller (1982). They converted their problem into a system of integro-differential equations which they solved under the conditions of small Weber numbers and large Reynolds numbers. The boundary element method for the potential problem has been extended to accommodate the effects of viscosity in a purely irrotational flow by Georgescu, Achard & Canot (2002) to study a gas bubble bursting at a free surface and by Canot *et al.* (2003) in their numerical simulation of

the buoyancy-driven bouncing of a two-dimensional bubble at a horizontal wall using the direct formulation of the boundary element method. Very recently, Gordillo (2008) studied the necking and break-up of a bubble under the action of gravity generated from a submerged vertical nozzle by modifying the code of RDZ for inviscid fluids to include the viscous effects of the irrotational motion of the liquid through the viscous normal stress at the interface, whereas the rotational effects in the gas (vorticity) are retained through a mechanistic model based upon the incompressible Navier–Stokes equations assuming a slender neck region that splits the gas pressure as an inviscid plus a viscous contribution. Predictions of the instantaneous position of the interface from this code are compared with those from a set of two-dimensional Rayleigh-like equations deduced with the assumption that the liquid velocity field is irrotational, and excellent agreement was found. These Rayleigh-like equations were used later by Bolanos-Jiménez *et al.* (2009) to study bubble pinch-off in liquids more viscous than water and good agreement with their experimental data was reported. They justified the hypothesis of an irrotational liquid velocity field by stating that 'the velocities induced by any of the possible sources of vorticity in our setup, i.e. the boundary layer at the needle wall and the interface curvature, are much smaller than the typical radial velocities associated to the collapse of the neck'.

Lundgren & Mansour (1988) also included the effect of a small viscosity by decomposing the velocity field into the sum of an irrotational and a rotational velocity, in which the former is expressed as the gradient of a potential and the latter is written as the curl of a vector potential. Substitution of this decomposition into the incompressible Navier–Stokes equations and applying order-of-magnitude arguments under the assumption of a thin vortical layer at the free surface of the drop yields a new set of differential equations for the potentials. These equations carry weak viscous effects and are coupled with the boundary integral formulation for potential flow based on the vortex method.

3. Problem formulation and numerical method

In what follows, we adopt the notation and the problem formulation of the analysis for inviscid fluids by RDZ for the most part. Differences with their formulation arise with the inclusion here of the viscous effects of the irrotational motion, which are not considered in their work. Regarding the numerical method, the algorithm we applied in this work follows the major steps of the algorithm presented by those authors. However, the numerical techniques applied here in the implementation of several of these steps differ from those employed by RDZ.

3.1. *Statement of the problem*

Consider a bubble or drop initially of spherical shape with radius a containing an incompressible Newtonian fluid of density ρ_i and viscosity μ_i and immersed in an unbounded incompressible Newtonian fluid of density ρ_e and viscosity μ_e. The entire smooth interface $\mathscr{S}$ is characterized by a uniform interfacial tension γ. It is assumed that the bubble or drop moves with the mean velocity of the flow. With respect to a reference frame that moves with this mean velocity, we describe the evolution of the bubble or drop interface as a result of a steady uniaxial extensional flow. That is, far away from the interface, the following velocity potential is prescribed

$$\hat{\phi}_\infty = \frac{M}{a}(2\hat{z}^2 - \hat{r}^2), \tag{3.1}$$

and the corresponding (irrotational) velocity field is $\hat{\boldsymbol{u}}_\infty = \hat{\nabla}\hat{\phi}_\infty$. We adopt a cylindrical coordinate system $(\hat{z}, \hat{r}, \zeta)$, in which the $\hat{z}$-axis is coincident with the axis

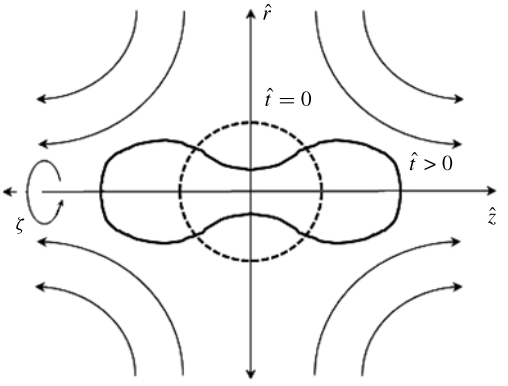

FIGURE 1. Two-phase flow system considered in this study: a bubble or drop of an incompressible fluid being deformed by an axially symmetric extensional incompressible flow. The shape of the interface is initially spherical.

of symmetry of the motion and $\hat{\zeta}$ is the azimuthal angle about the $\hat{z}$-axis (figure 1). From the potential in (3.1), the strain rate along the $\hat{z}$-direction, which is a principal direction, is $\partial^2\hat{\phi}/\partial\hat{z}^2 = 4M/a$, whereas the strain rates along the other two principal axes are the same and equal to $-2M/a$. Thus, the parameter M determines the magnitude of the principal strain rates. In formulating the problem, we also make the usual assumption of neglecting the effects of gravity including those associated with the variation of the hydrostatic pressure. This is a necessary condition for the interface deformation to be axisymmetric as discussed in Ramaswamy & Leal (1997). In order to write the governing equations in dimensionless form, the magnitudes a, $a/(8M)$ and $\rho_e\,(8M)^2$ are adopted as the characteristic length, time and pressure scales, respectively.

We also assume that the internal to external velocity fields are irrotational for all times. Hence, conservation of mass leads to a pair of Laplace's equations

$$\nabla^2\phi_i = 0, \quad \nabla^2\phi_e = 0, \tag{3.2}$$

where the subscripts i and e denote the internal and external fluids, respectively. Dimensionless variables are written with no '$\hat{}$'. For the irrotational motion of a viscous fluid, conservation of linear momentum is given by the Bernoulli's equation

$$\Lambda\left(\frac{\partial\phi_i}{\partial t} + \frac{|\nabla\phi_i|^2}{2}\right) + p_i = 0, \quad \frac{\partial\phi_e}{\partial t} + \frac{|\nabla\phi_e|^2}{2} + p_e = 0, \tag{3.3}$$

for the internal and external flows, respectively, and $\Lambda = \rho_i/\rho_e$. The solution of (3.2) and (3.3) must satisfy the following boundary conditions for points at the interface

$$\frac{\partial\phi_i}{\partial n_i} = -\frac{\partial\phi_e}{\partial n_e}, \tag{3.4}$$

$$\left[-p_e + \frac{2}{Re}\frac{\partial^2\phi_e}{\partial n_i^2}\right] - \left[-p_i + \frac{2\beta}{Re}\frac{\partial^2\phi_i}{\partial n_i^2}\right] = \frac{1}{We}\nabla_{\|}\cdot\boldsymbol{n}_i, \tag{3.5}$$

where the former establishes continuity of the normal velocity across the interface and the latter expresses that the jump of normal stresses across the interface is balanced by surface tension forces. Here, $\beta = \mu_i/\mu_e$, and the dimensionless numbers

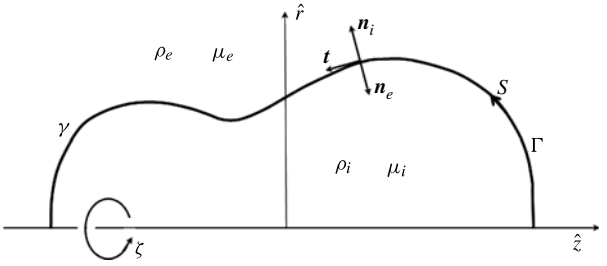

FIGURE 2. Sketch of the axially symmetric domain showing the cylindrical coordinate system $(\hat{z}, \hat{r}, \zeta)$ and the local orthogonal curvilinear coordinate system (n_i, s, ζ). Curve Γ represents the intersection of the axisymmetric interface $\mathscr{S}$ with a plane containing the $\hat{z}$-axis. The material properties of the internal and external fluids, as defined in § 3.1, are included.

$Re = \rho_e(8M)a/\mu_e$ and $We = \rho_e(8M)^2 a/\gamma$ are the Reynolds and Weber numbers, respectively. The first number represents the ratio of inertia to viscous forces and the second represents the ratio of inertia to surface tension forces. In (3.4) and (3.5), $\boldsymbol{n}_i$ is the unit vector normal to the interface pointing away from the internal fluid and $\boldsymbol{n}_e$ is the unit vector normal to the interface pointing towards the internal fluid, thus $\boldsymbol{n}_i = -\boldsymbol{n}_e$ (figure 2). Moreover, n_i (n_e) is the dimensionless coordinate along and increasing in the direction of $\boldsymbol{n}_i$ $(\boldsymbol{n}_e)$. Note that the term added to the pressure within the brackets corresponds to the viscous normal stress on this or that side of interface $\mathscr{S}$. Obviously, these terms, which account for the viscous effects of the irrotational motion, were not considered in the analysis for inviscid fluids by RDZ. The term $-\nabla_\parallel \cdot \boldsymbol{n}_i$ equals twice the mean curvature κ of the surface at a point, where $\nabla_\parallel(\ )$ is the surface gradient operator, $\nabla_\parallel = \nabla - \boldsymbol{n}(\boldsymbol{n}\cdot\nabla)$ (Joseph & Renardy 1993). Note that $\nabla_\parallel \cdot \boldsymbol{n}_i = \nabla \cdot \boldsymbol{n}_i$. By introducing a local orthogonal coordinate system (n_i, s, φ), where s is the arc-length of the plane curve Γ representing the interface increasing counterclockwise, and n_i and φ have been already defined, we write expressions in appendix A for the viscous normal stress and the mean curvature both needed in (3.5).

Turning now to the evolution of the interface, let $\boldsymbol{u}_{\mathscr{S}} = \mathrm{d}\boldsymbol{x}/\mathrm{d}t$ be the velocity of the interface $\mathscr{S}$ at point $\boldsymbol{x}$. With $\boldsymbol{u}_{\mathscr{S}} \cdot \boldsymbol{n}_i = \partial\phi/\partial n_i = \partial\phi_i/\partial n_i = \partial\phi_e/\partial n_i$ by continuity of the normal velocity component, and setting $\boldsymbol{u}_{\mathscr{S}} \cdot \boldsymbol{t} = 0$ arbitrarily because this tangential component is irrelevant in tracking the motion of the interface (Joseph *et al.* 2007), $\boldsymbol{t}$ being the unit vector tangential to $\mathscr{S}$ along the s direction, the position of the surface can be obtained from the equation

$$\frac{\mathrm{d}\boldsymbol{x}}{\mathrm{d}t} = \frac{\partial\phi}{\partial n_i}\boldsymbol{n}_i, \quad \boldsymbol{x} \in \mathscr{S}. \tag{3.6}$$

Therefore, points at the interface evolved in time by moving them normal to the interface. Other choices are found in the literature for the tangential velocity $\boldsymbol{u}_{\mathscr{S}} \cdot \boldsymbol{t}$. For instance, Heister (1997) set this value equal to the tangential velocity of the internal fluid at the boundary, whereas Leppinen & Lister (2003) used the average of the internal and external fluid tangential velocities. For irrotational motion, continuity of tangential velocities and stresses cannot be enforced.

Finally, in the far field $|\boldsymbol{x}| \to \infty$,

$$\phi_e \to \phi_\infty(z, r) = \frac{z^2}{4} - \frac{r^2}{8}. \tag{3.7}$$

The set of equations (3.2)–(3.3), together with boundary conditions (3.4), (3.5), (3.6) and (3.7) describe the evolution of the interface of the bubble or drop starting from an initial state that has $\mathscr{S}$ as a sphere of unit radius. The prescription of the initial conditions is discussed below. Note that the dimensionless parameters governing the problem are the Reynolds number Re, the Weber number We, the density ratio Λ and viscosity ratio β, and need to be prescribed.

We may write two scalar equations resulting from the projection of the kinematic condition (3.6) onto the axial and radial directions, respectively. This leads to

$$\frac{\mathrm{d}z}{\mathrm{d}t} = n_i^z \frac{\partial \phi}{\partial n_i}, \quad \frac{\mathrm{d}r}{\mathrm{d}t} = n_i^r \frac{\partial \phi}{\partial n_i}. \tag{3.8}$$

To track the time evolution of a scalar field defined on points moving with the interface, let us consider f to be any smooth field defined on a domain enclosing the entire interface $\mathscr{S}$. If $\boldsymbol{x}$ is a point on the interface, differentiation of $f(\boldsymbol{x}(t), t)$ with respect to time yields

$$\frac{\mathrm{d}f}{\mathrm{d}t} = \frac{\partial f}{\partial t} + \boldsymbol{u}_{\mathscr{S}} \cdot \nabla f = \frac{\partial f}{\partial t} + (\boldsymbol{u}_{\mathscr{S}} \cdot \boldsymbol{n}_i)\boldsymbol{n}_i \cdot \nabla f = \frac{\partial f}{\partial t} + \frac{\partial \phi}{\partial n_i}\frac{\partial f}{\partial n_i}. \tag{3.9}$$

Expression (3.9) establishes that quantities for points at the interface are advected by the normal component of the velocity.

Suppose now that velocity potentials $\phi_{(i,e)}$ both belong to the same class of functions as f. Therefore, by expression (3.9) and continuity of normal velocities, we can write

$$\frac{\mathrm{d}\phi_{(i,e)}}{\mathrm{d}t} = \frac{\partial \phi_{(i,e)}}{\partial t} + \left(\frac{\partial \phi}{\partial n_i}\right)^2. \tag{3.10}$$

Introducing the difference function,

$$\varphi \equiv \phi_e - \Lambda \phi_i, \tag{3.11}$$

and eliminating the pressures in (3.5) by the use of Bernoulli's equations (3.3), we find, after rearranging terms using (3.10),

$$\begin{aligned}\frac{\mathrm{d}\varphi}{\mathrm{d}t} = {} & \frac{1}{We}\nabla_{\parallel} \cdot \boldsymbol{n}_i + \frac{1}{2}(1-\Lambda)\left(\frac{\partial \phi}{\partial n_i}\right)^2 - \frac{1}{2}\left[\left(\frac{\partial \phi_e}{\partial s}\right)^2 - \Lambda\left(\frac{\partial \phi_i}{\partial s}\right)^2\right] \\ & - \frac{2}{Re}\left[\frac{\partial^2 \phi_e}{\partial n_i^2} - \beta\frac{\partial^2 \phi_i}{\partial n_i^2}\right],\end{aligned} \tag{3.12}$$

for the rate of change of φ for points on the interface that advance in time according to (3.8).

Integration of the set of differential equations (3.8) and (3.12) gives the shape of the interface after start-up. In order to solve this system of equations, we prescribe an initial shape and the distribution of φ on the interface. Initially, we consider the bubble (drop) to have a spherical interface. For φ, we choose

$$\varphi = 0. \tag{3.13}$$

This choice is such that the potentials at the interface does not exhibit an abrupt change with time at the instant in which the potential in the far field jumps from a constant to the value given in (3.1) for a uniaxial extensional flow.

The set of equations (3.8) and (3.12) can be integrated numerically with initial condition (3.13) and the boundary points (z, r) starting from the semicircumference

$z^2 + r^2 = 1$, $r \geqslant 0$, to track the deformation of the interface as time advances. To compute the right-hand side of (3.8) and (3.12), the distribution of the potentials ϕ_i and ϕ_e, and the normal derivative $\partial\phi/\partial n_i$ are needed. This motivates the reformulation of Laplace's equations (3.2) as boundary integral equations using Green's representation formula for both the internal and external domains. These integral equations involve information only at the boundary an therefore reduce the dimensionality of the problem. For expressions (3.2), with boundary conditions (3.4) and (3.7), and considering the axial symmetry of the problem, the boundary integral equations have been presented in RDZ and hence are not written here. Knowing the position of the boundary and the distribution of φ on it, at a given time, suffices to determine, via the boundary integral equations, the distribution of potentials and their normal derivative for points on the boundary.

3.2. *Numerical method*

Considering that the bubble or drop will undergo large deformations depicting somewhat complex shapes driven by the uniaxial extensional flow imposed in the far field, the solution of the system of equations established in § 3.1 must be sought by numerical means. In this section, we describe how the approximate solution methods for these equations may be implemented in a computer program. This program will perform three major tasks, as follows:

(i) Implementation of the boundary element method to solve the system of integral equations for the fluids normal velocity component at the interface and potentials on both sides of the interface at a given time. This requires discretization of the interface by dividing it into segments joined by nodal points; interpolation of the geometry, potential and normal derivative of the potential; numerical evaluation of the integrals, and assembling and solution of two linear systems of algebraic equations obtained with the collocation method.

(ii) Numerical integration of the system of differential equations governing the time evolution of discrete points on the interface to obtain its position at discrete times. A Runge–Kutta fourth-order scheme with adaptive time stepping is implemented in this stage.

(iii) Refinement and smoothing of the grid to improve resolution in regions of the curve approaching the axis of symmetry when pinch-off is imminent and to avoid interfacial instabilities of numerical origin.

These stages are coupled. The solution of the potential problem as described in the first task must be accomplished for each time step. Its results are used in the time integration procedure to march to the next time level. Then, the updated boundary position and potential distribution are inputs for the potential problem solver to perform again and a cycle is established. Refinement and smoothing of the mesh does not necessarily occur after each time step.

Here, we adopt the general algorithm originally presented by RDZ with several modifications in the details of its implementation. In various parts of the procedure, we make choices of numerical methods that differ from those selected by those authors. The reader is referred to Padrino (2010) where the complete details on the implementation of the stages listed above are described.

To compute the integrals arising in the boundary element method, the potential and normal derivative are assumed to vary linearly within an element with the arc-length coordinate, s. Quintic splines are used to interpolate the spatial coordinates. The sum of the distance between consecutive nodes is used as a spline parameter. Four

end conditions are required to compute the splines: the z coordinate must satisfy $\mathrm{d}z/\mathrm{d}\ell = \mathrm{d}^3z/\mathrm{d}\ell^3 = 0$ at both ends, whereas, for the r coordinate, $\mathrm{d}^2r/\mathrm{d}\ell^2 = \mathrm{d}^4r/\mathrm{d}\ell^4 = 0$. Here, ℓ denotes the spline parameter. A linear system of equations is formed by applying the collocation method. Well-known fits for the complete elliptic integral appearing in the axisymmetric kernels of the boundary integral equations are employed (Abramowitz & Stegun 1964). When the collocation point belongs to the element over which the integration is being carried out, a weak (logarithmic) singularity arises from the complete elliptic integral of the first kind. These singular integrals are computed with the special logarithmic quadrature using six points (Stroud & Secrest 1966). For the non-singular (regular) integrals, standard Gauss–Legendre quadrature with six points is applied. Since the matrices appearing in the boundary element method are fully populated, the linear systems are solved using LU decomposition. The derivatives of the potential needed in (3.8) and (3.12) are computed using a quintic spline interpolation with end conditions as for the z coordinate. Rodríguez-Rodríguez *et al.* (2006) reported the use of quartic splines for interpolation and the singularity substraction technique for the weakly singular integrals.

Owing to the initial shape and the boundary conditions satisfied by the solution of the problem subject of analysis, the flow field is symmetric with respect to the plane $z = 0$. Therefore, one can substantially reduce the computational effort needed in the solution of the linear systems by enforcing equatorial symmetry in the geometry coordinates, potentials $\phi_{(i,e)}$ and normal velocity $\partial\phi/\partial n_i$. In this work we have two versions of the boundary element method algorithm, namely, one in which equatorial symmetry is not assumed and another in which equatorial symmetry is enforced (see also the discussion below).

The time step is dynamically modified in order to properly resolve the shape of the interface when approaching pinch-off and its value is found by requiring that no nodal point will move beyond a fraction of the smallest element size. This time step cannot be larger than the time step needed to resolve inviscid capillary waves with the smallest grid dimension (Leppinen & Lister 2003).

It is desirable to have grid refinement by having shorter separation between nodes in particular regions of the boundary. This allows for greater detail in the resolution of the shape of the boundary at the instants before pinch-off. In the present computations, we adopt a refinement scheme similar to that of Leppinen & Lister (2003). Interpolating the coordinates of the nodes on the boundary using quintic splines, the separation between adjacent nodal points $\{\boldsymbol{x}_j, \boldsymbol{x}_{j+1}\}$ was set to $0.1D$, where D is the distance between point $\boldsymbol{x}_j$ and the point $(z_{min}, 0)$ where (z_{min}, r_{min}) are the coordinates of the nodal point on the interface with the minimum radius in the neck region, that is, the node closest to the axis of symmetry in the neck, when this region appears. In this notation, the index $j = 1$ corresponds to the node with coordinates (z_{min}, r_{min}) and increases towards both ends of the boundary. This grid spacing was restricted to be no larger than an upper bound defined as an input to the code. This grid refinement strategy was applied in the version of the code for which equatorial symmetry was considered in the solution of the discrete boundary integral equation. This version of the code is used in the case of a drop, where break-up takes place, because of symmetry, simultaneously at two different points away from the plane $z = 0$ in the cases considered in this work. In the version of the code that does not enforce equatorial symmetry, the grid refinement strategy described above is modified by setting $z_{min} = 0$ for all times, this abscissa being associated with the node $N/2 + 1$, with N being the (even) total number of elements. This version of the code is used to

simulate the deformation of a bubble, i.e. small Λ, in which case the minimum radius of the neck is expected to be located at $z_{min} = 0$.

The grid refinement method has been combined with the smoothing strategy of node staggering in a manner similar to that implemented by Oguz & Prosperetti (1990). The staggering technique is applied to prevent the development of 'zig-zag' instabilities on the interface when simulations run for relatively long time intervals (Longuet-Higgins & Cokelet 1976; Lundgren & Mansour 1988; Hilbing, Heister & Spangler 1995; Heister 1997). Filtering schemes based on fast Fourier transforms that eliminates high-frequency components, which were used by RDZ, are not employed in our program.

The scheme described above is implemented as a sequential code; it was run in a single node of a 307-node cluster, each containing two dual-core 2.6 GHz processors sharing 8 GB of main memory.

4. Results and discussion

The problem described in § 3.1 is solved numerically using the procedure detailed in § 3.2. Here, we present and discuss the results of the simulations for the case of a bubble, for which the density ratio is very small, and for the case of a drop, for which the density ratio is $O(1)$. Before doing so, we discuss the validation stage for the numerical method employed.

4.1. *Validation of the numerical set-up*

The validation of the axisymmetric solver is carried out first by comparing its predictions with analytic results for the small oscillations of a bubble or drop about the spherical shape from both inviscid (Lamb 1932) and viscous potential flow (Joseph *et al.* 2007; Padrino, Funada & Joseph 2008). In this case the motion is driven by capillary forces as a result of an initial deformation imposed on the interface in the absence of any prescribed flow in the far field. The dimensionless equations presented in § 3.1 are still valid for this setting. However, since the flow strength $M = 0$ in the far field, one must choose a different velocity scale, $\sqrt{\gamma/(\rho_e a)}$ in this case, so that the Weber number is now fixed, $We = 1$, and the Reynolds number is $Re = \sqrt{\rho_e \gamma a}/\mu_e$, which is simply Oh_e^{-1}, where Oh_e is the Ohnesorge number for the exterior fluid. Two independent modes of oscillation are considered, namely, the second and fourth modes, which are set by an initial interfacial shape of the form $1 + \epsilon P_n(\cos\theta)$ with $n = 2$ and 4, respectively, and ϵ is a 'small' number; P_n are the Legendre polynomials of order n. With these modes, the interface evolves preserving equatorial symmetry.

Figure 3 shows the variation with time of the normalized amplitude of the right end of the bubble or drop obtained with the numerical method presented above for both inviscid and viscous fluids and 128 elements. In the latter case, we chose $Re = 100$ and a viscosity ratio $\beta = 0.01$ for the bubble and $\beta = 0.1$ for the drop. These choices give a decay rate such that the interface oscillates over several time periods without decaying too fast, thereby allowing the analysis of the signal. Figure 3(*a*) and (*b*) correspond to the second mode and $\epsilon = 0.05$, whereas figure 3(*c*) and (*d*) correspond to the fourth mode and $\epsilon = -0.05$. Density ratio in these cases is $\Lambda = 0.0012$ (bubble case). The frequency of oscillations increases by increasing n. In the inviscid case (figure 3*a* and *c*), nonlinear effects can presumably be observed as the amplitude of the oscillations slightly deviates from a constant value. In figure 3(*e–f*) the initial deviation of the bubble interface is reduced (in absolute value) to $\epsilon = -0.005$. By comparing figure 3(*c*) and (*e*), one can note that the amplitude of the oscillations tend

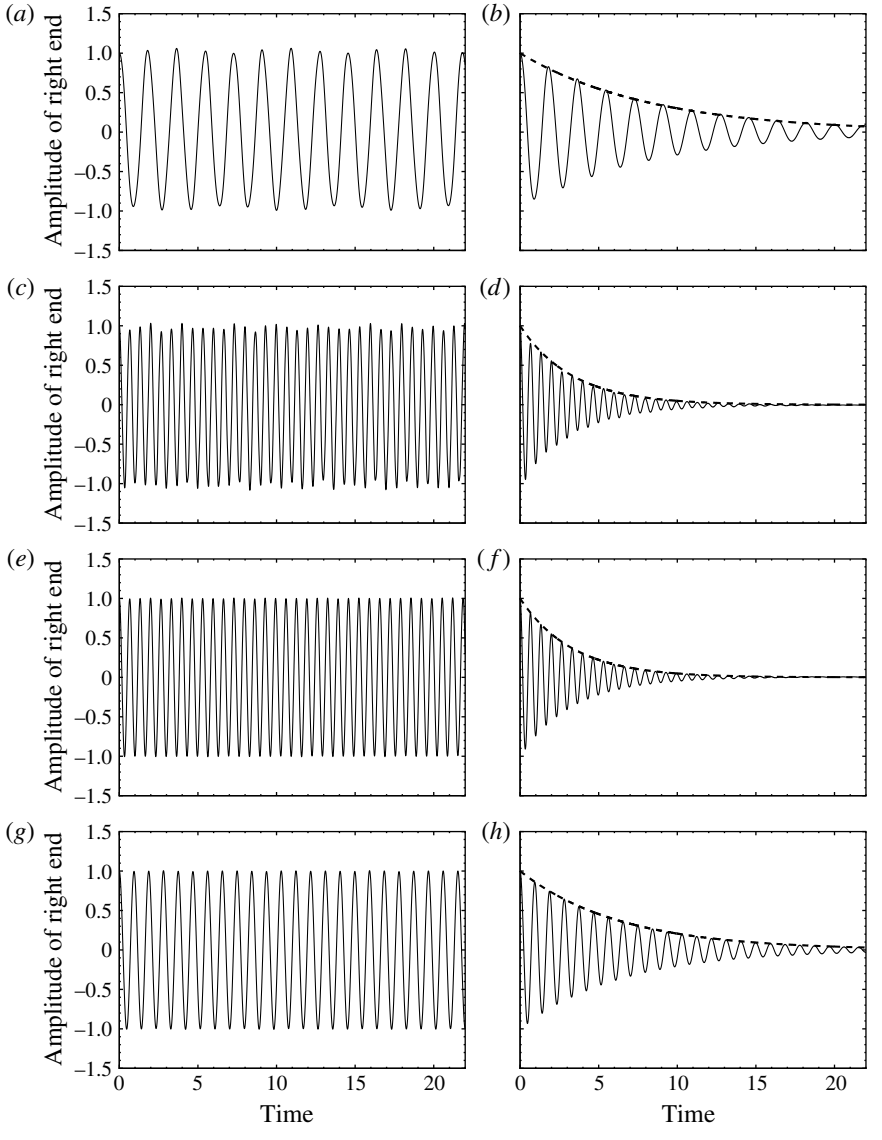

FIGURE 3. Amplitude of the right end of the bubble or drop $z_{end}(t) = |\boldsymbol{x}_{end}(t)|$, where $\boldsymbol{x}_{end}(t) = (z(t), 0)$, as a function of time. This amplitude is presented in normalized fashion, $(z_{end}(t) - 1)/\epsilon$. The motion of the system is due to an initial perturbation of the spherical interface of unit radius given by $|\boldsymbol{x}(0)| = 1 + \epsilon P_n(\cos\theta)$, where P_n are the Legendre polynomials of order either $n = 2$ or 4, and θ is the polar angle. The fluid is at rest in the far field. The figures on the left correspond to inviscid potential flow, whereas the figures on the right result from viscous potential flow simulations with a Reynolds number $Re = 100$. Panels (*a*) and (*b*) are obtained with $n = 2$, $\epsilon = 0.05$ and density ratio $\Lambda = 0.0012$ (bubble). For panels (*c*) and (*d*), $n = 4$, $\epsilon = -0.05$ and $\Lambda = 0.0012$, whereas for panels (*e*) and (*f*), $n = 4$, a much smaller (in absolute value) deviation $\epsilon = -0.005$ and $\Lambda = 0.0012$. Panels (*g*) and (*h*) results from $n = 4$, $\epsilon = -0.005$ and $\Lambda = 0.8$ (drop). The frequency and decay rate of the oscillations are compared with the linear, viscous potential flow theory, from which the dashed lines shown in the figures on the right are obtained.

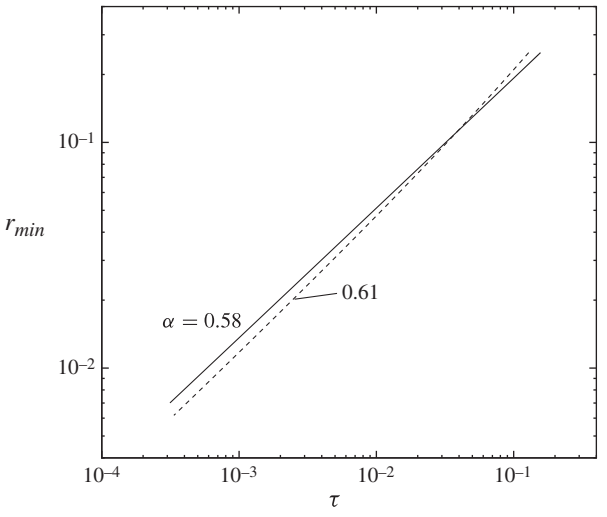

FIGURE 4. Minimum neck radius r_{min} as a function of the time to break-up $\tau = t_b - t$ for a bubble in uniaxial straining motion; the density ratio $\Lambda = 0.0012$ and the fluids are inviscid. For the interval shown, the fit of the scaling $r_{min} \sim \tau^{\alpha}$ is presented, where α is an 'effective' exponent. The thin solid line corresponds to a Weber number $We = 10$ and the dashed line corresponds to $We \to \infty$.

to a constant value as ϵ becomes smaller in the inviscid case. Finally, figure 3(*g*) and (*h*) show the change in amplitude for a drop ($\Lambda = 0.8$), $n = 4$ and $\epsilon = -0.005$. Results for a drop and $\epsilon = -0.05$ were also obtained but are not shown here as they conform to those results already depicted. In all of the cases, the frequency of the oscillations shows excellent agreement with the theoretical results obtained in the linearized case by Lamb (1932) for fluids with zero viscosity and by Joseph *et al.* (2007) for two viscous fluids (see Padrino *et al.* 2008). The relative error in all of the cases lies within 0.4 %. In the viscous case, figure 3 also demonstrates a very good match between the theoretical and numerical results for the decay rate of the oscillations.

This is perhaps the first time in which the linear viscous potential flow theory for the small oscillations of a bubble or drop is used to validate a numerical method developed to solve the nonlinear deformation of an interface shared by two viscous fluids whose motion is assumed to be irrotational. The linear inviscid theoretical result by Lamb (1932) has been used elsewhere to validate, in the small deformation case, algorithms solving boundary integral equations to simulate the inviscid motion of an interface or free surface (Hilbing *et al.* 1995; RDZ). It should also be mentioned that Lundgren & Mansour (1988) used a boundary integral formulation to study the oscillations of a drop with 'weak' viscous effects. Their formulation, which differs from the viscous potential flow approach followed here, was validated using the result from Lamb's viscous dissipation approximation. The viscous dissipation approximation is different from the linearized viscous potential flow method employed in the present validation and, therefore, one should not expect agreement between results from these two methods.

Nonlinear (large) deformations of a bubble ($\Lambda = 0.0012$) or a drop ($\Lambda = 0.8$) in a uniaxial extensional motion according to the problem formulation in § 3.1 for inviscid fluids are computed with the algorithm described here and compared in appendix B with results obtained by RDZ, where excellent agreement is shown. In figure 4 we

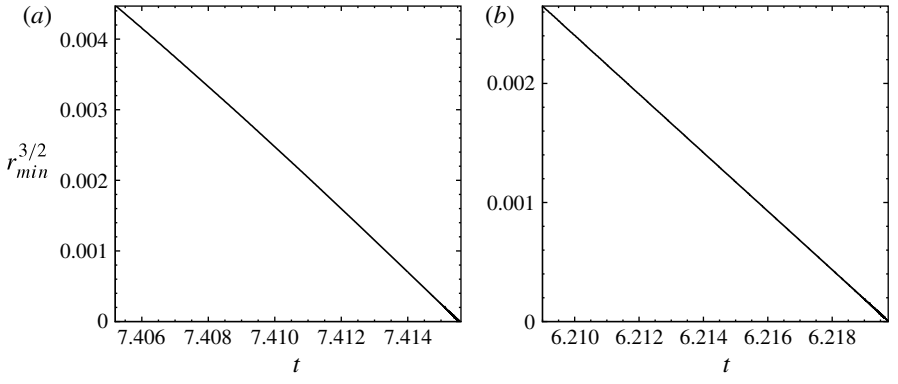

FIGURE 5. Power of the minimum neck radius $r_{min}^{3/2}$ as a function of time t approaching pinch-off for an inviscid drop within another inviscid liquid with density ratio $\Lambda = 0.8$ and Weber number (*a*) $We = 3$ and (*b*) $We = 10$. The figures show that the minimum neck radius approaches pinch-off following the scaling $r_{min} \sim \tau^{2/3}$ as the time to pinch-off $\tau = t_b - t \to 0$.

show the variation of the minimum neck radius r_{min} with the time to break-up $\tau = t_b - t$ for a bubble neglecting the fluids viscosity; here, t_b is the break-up time. The fitting of the law $r_{min} \sim \tau^{\alpha}$, where α is an effective exponent, gives rise to values of α somewhat larger than 0.5, as expected (Gordillo *et al.* 2005), and closer to values determined from experimental data for a bubble detaching from a nozzle due to gravity ($\alpha = 0.56$ by Keim *et al.* 2006 and $\alpha = 0.57$ by Thoroddsen, Etoh & Takehara 2007). The slight difference with our results may be due to the fact that their experimental setting is different from the configuration studied here, as the precise value of α depends on the initial and boundary conditions and also, perhaps, to the range of r_{min} fitted in these graphs. We note that the ranges plotted here for τ and r_{min} are similar to those used by Gordillo *et al.* (2005).

The evolution of the neck minimum radius r_{min} as pinch-off is approached for a drop ($\Lambda = 0.8$) is shown to follow the law $r_{min} = \tau^{2/3}$ in figure 5 for the time interval considered for both Weber numbers $We = 3$ and 10 in agreement with analyses and numerical predictions (Keller & Miksis 1983; Chen & Steen 1997; Day, Hinch & Lister 1998; Leppinen & Lister 2003). Here, we show only the cone to the right of the equatorial plane $z = 0$. In the initial stages of the deformation, a local minimum appears at the equatorial plane ($z = 0$). At a certain time, the interface local minimum is shifted out of this plane yielding two new local minima, having the same radial coordinate, at positions that are symmetric with respect to the equatorial plane. This is illustrated in figures 11 and 17, where the evolution of the shape of a drop is shown. For a drop and $We = 3$, figure 6(*a*) shows the evolution of the interface in the neck region as it approaches pinch-off. Note that the interface overturned before breaking up and so both the steep and shallow parts of the interface being connected by the necking region depict negative slopes with respect to the reference frame shown. As time progresses, the interface tend to attain a cone shape about the minimum radius and $r_{min} \to 0$ in a finite time creating a kink. Also note the dense grid for the last instant included in the figure, for which the interface is discretized by 605 nodal points (initially we set 129 nodes) and the final (adaptive) time steps are of order 3×10^{-9}. In figure 6(*b*), we present the scaled profiles near drop pinch-off r_s versus z_s using the coordinates of the neck (z_{min}, r_{min}) as indicated in the figure's caption at each instant depicted. With this new set of coordinates the profiles show a clear tendency

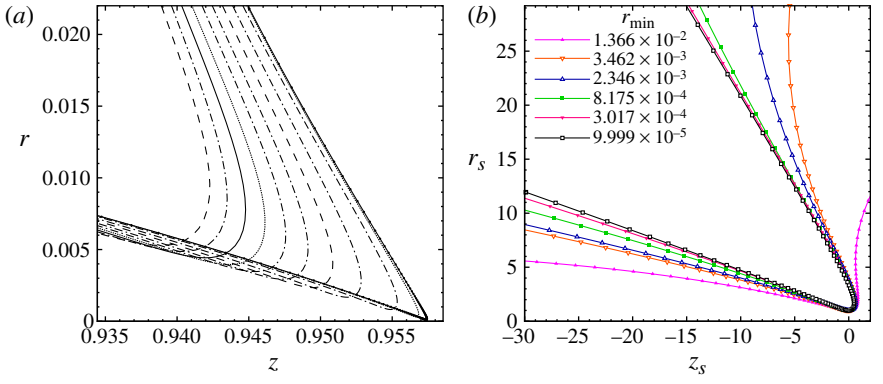

FIGURE 6. (Colour online available at journals.cambridge.org/flm) Interface shapes for various times approaching pinch-off for a drop of an inviscid fluid in another inviscid liquid; the density ratio is $\Lambda = 0.8$ and the Weber number is $We = 3$. In panel (a) the coordinates r versus z are shown; for the last instant, the node distribution over the interface is depicted, highlighting the high nodal density of the grid around the neck region. In panel (b) the shapes tend to collapse onto a conical shape when rescaled with the minimum neck radius r_{min} and centred on z_{min}, i.e. $z_s = (z - z_{min})/r_{min}$ and $r_s = r/r_{min}$, thereby suggesting self-similarity. Two decades of variation of r_{min} with time are shown in the legend.

to collapse onto a single smooth curve as the time to break-up τ and thus r_{min} both go to zero; therefore, in this scaled set of coordinates, this inviscid break-up process is self-similar, as expected (Leppinen & Lister 2003). It should be mentioned that tests have been conducted by duplicating the initial number of elements and refining further the spatial and temporal discretizations near break-up for the cases leading to figures 5 and 6 and the new graphs do not overlap with those shown in figure 5 but some discrepancy is obtained. Therefore, the results presented in figures 5 and 6 should be taken with some caution. Nevertheless, the scaling law $r_{min} \sim \tau^{2/3}$ is maintained. We emphasize that the description of the evolution of the interface from a macroscopic point of view and the prediction of the break-up time with the viscous potential flow theory are the central features of our study. The focus is not the description of the local dynamics of the necking region when pinch-off is imminent. To undertake such an analysis, one may need to implement improved interpolation methods for the variables at the interface and perhaps more sophisticated refinements techniques for positioning the nodes.

4.2. *Bubble analysis for viscous fluids*

In this section, the time evolution of the interface of a bubble in a uniaxial extensional flow is computed using the numerical method described in § 3.2 considering irrotational motion and the internal and external fluids to be viscous. The goal is to compare the results obtained here under these assumptions with the results given very recently by REV from the numerical solution of the incompressible, fully viscous Navier–Stokes equations using a projection method with suitable spatial and time discretizations of the various terms combined with a level set method to track the evolution of the interface. They dimensionalized their governing equations with the same scales as those used in § 3.1. In their numerical study, the initially spherical bubble starts from rest, the density and viscosity ratios $\Lambda = 0.001$ and $\beta = 0.01$ and the remaining controlling parameters, i.e. the Reynolds and Weber numbers, as defined

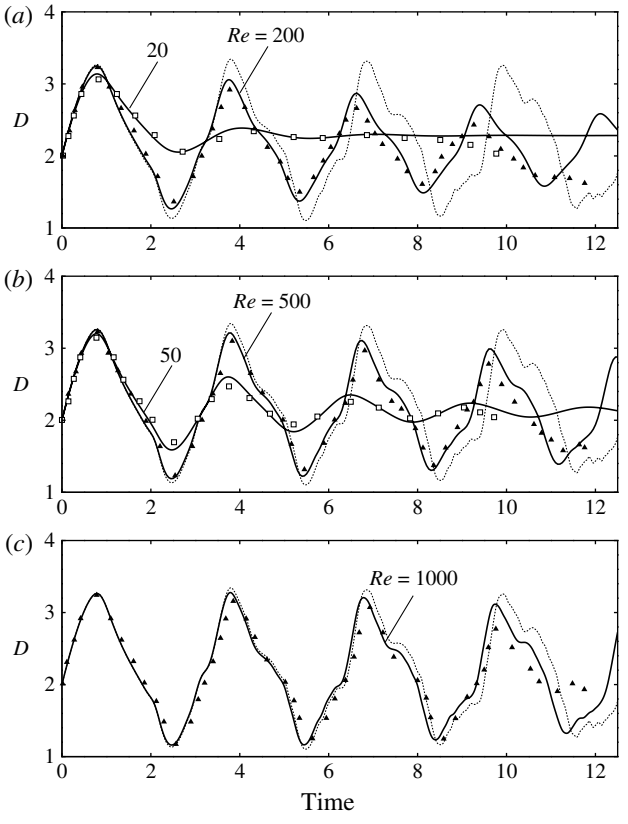

FIGURE 7. Total bubble axial dimension D as a function of time for various Reynolds numbers Re and a subcritical Weber number, $We = 1.5$. Here, the density ratio $\Lambda = 0.001$ and viscosity ratio $\beta = 0.01$. The bubble shows an oscillatory motion with large amplitude. Decreasing the Reynolds number significantly damps the amplitude of the oscillations until steady state is reached. Therefore, the bubble reaches steady state faster for the lowest Re. Solid line, viscous potential flow results from the present work; dotted line, inviscid potential flow results from the present work; symbols, results from simulations of the fully viscous Navier–Stokes equations by REV, where ▲ corresponds to the highest Re and □ to the smallest. Very good agreement is observed between these two approaches.

in § 3.1, take different values. REV point out that the errors in the computation of the (bubble) mass were within 1 %, except for high Reynolds numbers and low Weber numbers, where the errors were within 3 %.

In figure 7, the change of the total axial dimension of the bubble D with time is presented for five different values of Re and also for the inviscid case, $Re \to \infty$, for a fixed $We = 1.5$. This magnitude is lower than the critical Weber number We_c above which inertia effects are strong enough to overcome the surface tension effects that tend to preserve the integrity of the bubble, thereby leading to break-up. REV found $We_c \approx 2.22 \pm 0.005$ and independent of Re for $Re \geqslant 20$. Therefore, for $We = 1.5$, the bubble does not break up. It is shown that the oscillations are more rapidly attenuated as the Reynolds number decreases as a result of viscous dissipation and the bubble shape quickly reaches steady state. The figures show very good agreement between the calculations from the potential flow of viscous fluids of the present work (solid lines) and the fully viscous Navier–Stokes equations by REV (symbols) for up to $t \approx 8$,

indicating that viscous effects are mostly associated with the irrotational motion during this stage. Because the initial condition is irrotational, the viscous results for the largest Reynolds numbers, i.e. $Re = 200$, 500 and 1000, match the inviscid solution, at least for the first cycle, as in the case of $Re = 200$. This is not the case for the smallest values of Re considered, $Re = 20$ and 50, for which discrepancies with the inviscid results are evident almost from the start. Finally, note that the results from the fully viscous Navier–Stokes equations seem to get damped abruptly, especially for the largest Re, a phenomenon that may be regarded as unexpected and it is not discussed by REV. In our numerical solutions for the subcritical cases, the maximum error in the computation of the volume of the bubble lies within 0.02 %. For the set of values of Re mentioned above, we conducted tests with our code and found about the same critical value We_c as that reported by REV, with a very weak dependence on Re. With respect to the trend for inviscid fluids, we expect that, theoretically, a true periodic regime be reached after several cycles. However, the error associated with a numerical approximation of the solution may prevent such a behaviour to occur (e.g. mass loss or gain as time progresses).

In passing, it should be mentioned that bubble break-up still may take place for subcritical $We < We_c$ if the strength M of the extensional flow in the far field is set to fluctuate and a mechanism of resonance occurs with the bubble oscillations (see Kang & Leal 1990; REV); however, this case is out of the scope of this research as the strength M does not change with time in the present analysis. Note also that REV predict that We_c decreases towards zero as $Re \to 0$. In comparing their critical values for We with those reported by Kang & Leal (1990) for intermediate and large Re, substantial discrepancies are obtained. REV explained these differences arguing that the initial conditions that they imposed and the criterion used to determine We_c are not the same as those used by Kang & Leal (1990).

Now turning our attention to the case of supercritical Weber numbers, figure 8 shows the break-up time t_b as a function of the Weber number We for several magnitudes of the Reynolds number Re obtained from the viscous potential flow computations. These predictions are compared with results from the solution of the fully viscous Navier–Stokes equations. In addition, results for inviscid fluids are also included. The vertical dashed-dotted line corresponds to the critical value reported by REV ($We_c = 2.22$). As explained above, for higher values of We the bubble breaks up. For $3 \leqslant We \leqslant 6$, predictions from both theories show very good agreement. This result is important because it is known (RDZ) that We of order 5 are found in practical applications (e.g. atomization). On the other hand, for $We > 6$, discrepancies become noticeable, with the largest differences found to be of 13 % for $Re = 20$, the smallest value used in the analysis, as expected. For the largest Re, differences between viscous potential theory and the results from the Navier–Stokes equations are small. Note that viscous potential flow underpredicts the break-up time, that is, the bubble breaks up in shorter time for viscous potential flow than for the motion resulting from the Navier–Stokes equations. Thus, as Re decreases and We increases, rotational effects (vorticity) generated at the interface become influential in the dynamics. From this figure, it is also evident that the break-up time increases as We decreases for fixed Re. Examining the results of REV one can notice that for the smallest Re considered in their work, a plateau is obtained in the graphs of break-up time versus We. That is, for fixed Re, there exists certain We above which break-up time becomes almost independent of the Weber number. This trend is not reproduced by the viscous potential flow results. It should be mentioned that the break-up time in most of the simulations presented in this work is obtained by stopping the computations when the

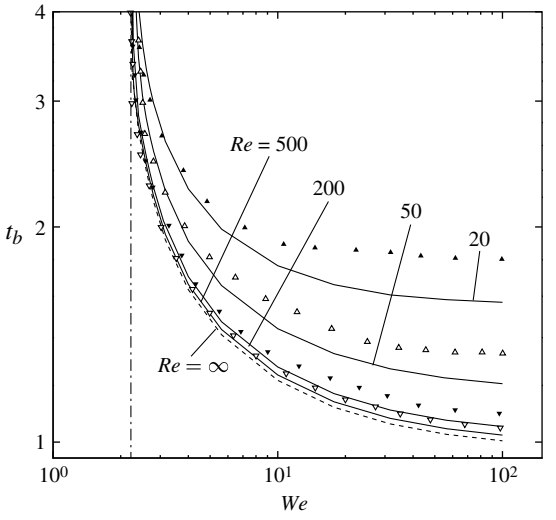

FIGURE 8. Bubble break-up time t_b as a function of the Weber number *We* for various Reynolds numbers *Re*. Here, the density ratio $\Lambda = 0.001$ and viscosity ratio $\beta = 0.01$. Solid line, viscous potential flow results from the present work; dashed line, inviscid potential flow results from the present work; symbols, results from simulations of the fully viscous Navier–Stokes equations by REV, where ▲ corresponds to $Re = 20$, △ to $Re = 50$, ▼ to $Re = 200$ and ▽ to $Re = 500$. The vertical dashed line represents the cross-over from a subcritical condition (no break-up) to a supercritical condition (break-up).

minimum radius in the neck region reaches $r_{min} < 2 \times 10^{-3}$ or, in some cases, 10^{-4}. For a typical initial bubble radius of the order of 1 mm, this criterion establishes a neck dimension smaller than 2 μm to stop the computations. The time for which the bubble or drop actually breaks up will be very shortly after the value determined by the criterion, because one expects the time to break-up to be of the order of or smaller than the minimum radius. In other words, continuing the computations beyond the aforementioned limit will not significantly modify the break-up time reported in the figures.

The time evolution of the bubble interface for different combinations of *Re* and *We* obtained with the method presented here is compared with the profiles presented by REV in figure 9. For the latter, three instants before pinch-off are presented. It should be mentioned that REV did not show the bubble interface at the instant of pinch-off, but *before* and *after* pinch-off (the latter is not reproduced here). Overall, the predictions from the boundary element formulation for viscous potential flow agrees well with the profiles given by the level set method used by REV coupled with a Navier–Stokes solver. In particular, the match is very good for the instants well before pinch-off as the effects of the vorticity created at the interface are still inconsequential. For cases (*a*), (*b*) and (*c*), our irrotational solution clearly underpredicts the break-up time; case (*a*), i.e. $Re = 50$ and $We = 50$, shows the most conspicuous difference since we predict $t_b = 1.235$ whereas computations by REV result in $1.32 < t_b < 1.4$. For case (*d*), however, the present computation predicts a larger break-up time $t_b = 2.78$, whereas REV indicate $2.65 < t_b < 2.72$. This is evidence that for supercritical *We* close to the critical value, there exists discrepancies between the viscous potential flow and the Navier–Stokes results. These differences are difficult to appreciate in figure 8.

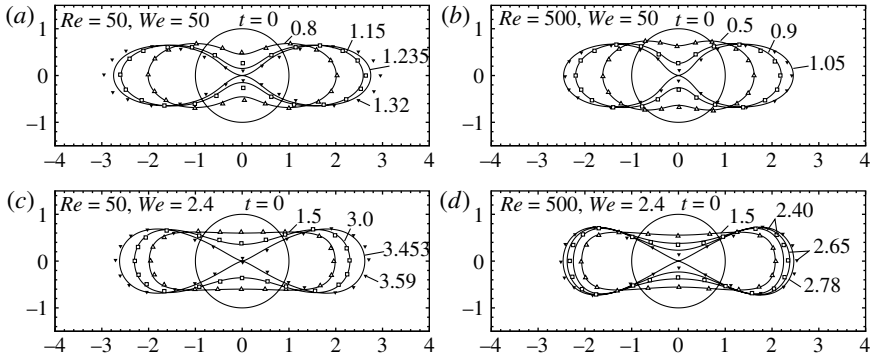

FIGURE 9. Bubble break-up profiles with density ratio $\Lambda = 0.001$, viscosity ratio $\beta = 0.01$, Reynolds numbers $Re = 50$ and 500 and Weber numbers $We = 2.4$ and 50. The solid lines represent results from the viscous potential flow analysis of the present work. Symbols correspond to results from simulations of the fully viscous Navier–Stokes equations given by REV. The profiles by REV for the last instant shown in the figures, and denoted by ▼, do not correspond to the instant of break-up.

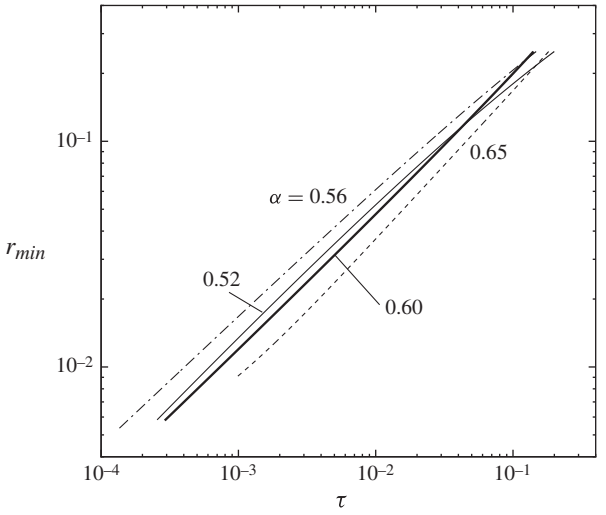

FIGURE 10. Minimum neck radius r_{min} as a function of the time to break-up $\tau = t_b - t$ for a bubble in uniaxial straining motion; the density ratio $\Lambda = 0.001$ and the fluids are viscous with viscosity ratio $\beta = 0.01$. For the interval considered in the figure, the fit of the scaling $r_{min} \sim \tau^{\alpha}$ is shown, where α is an 'effective' exponent. The thin solid line corresponds to a Reynolds number $Re = 50$ and Weber number $We = 2.4$; the dashed line corresponds to $Re = 50$ and $We = 50$; the dash-dotted line corresponds to $Re = 500$ and $We = 2.4$; and the thick solid line corresponds to $Re = 500$ and $We = 50$.

In figure 10, graphs of minimum neck radius r_{min} as a function of τ are shown when the interface approaches pinch-off for four cases corresponding to supercritical conditions that combine the values $Re = 50$ and $Re = 500$, with $We = 2.4$ and $We = 50$. For the interval plotted, a fit of the relation $r_{min} \sim \tau^{\alpha}$ is shown, with the 'effective' coefficient α ranging between 0.52 and 0.65. For $We = 50$, when Re decreases from 500 to 50 (i.e. increasing liquid viscosity with everything else fixed, including

interfacial tension), the exponent increases from $\alpha = 0.60$ to 0.65, a result that follows a tendency observed in numerical simulations performed for a bubble detaching from a nozzle due to gravity (Quan & Hua 2008). Although we are comparing different physical settings, the exponents α follow a similar tendency here and there. In any case, as mentioned above, α depends on the initial and boundary conditions (Bolanos-Jiménez *et al.* 2009). The increment of α with liquid viscosity has been obtained in experiments for a bubble coming out of a nozzle (Burton, Waldrep & Taborek 2005; Thoroddsen *et al.* 2007; Bolanos-Jiménez *et al.* 2009), even though in this case surface tension might vary as the liquids are changed to modify the viscosity. In contrast, for $We = 2.4$, decreasing Re also reduces the exponent α; we argue that this trend is due to the fact that this We is close to the critical value and thus the break-up times are longer (see figures 8 and 9), and the effects of the vorticity might therefore become important. Note also that when the strain rate, fluid densities and viscosities and bubble initial radius are held fixed and surface tension decreases, We increases with Re fixed and our model predicts an increment in α, a trend that agrees with previous numerical results for the collapse of a bubble coming out of a nozzle (Quan & Hua 2008).

4.3. *Drop analysis for viscous fluids*

In this section we present results for the deformation of a drop in the uniaxial straining flow of a liquid. In this case, we set $\Lambda = 0.8$. The results discussed here are obtained from the viscous potential flow approach and the numerical method of § 3.2. No comparison is presented for the evolution of the drop interface computed here with profiles resulting from numerical solutions of the *unsteady* incompressible Navier–Stokes equations, since, unexpectedly, this type of computation has not been found in the literature, as commented in § 1.

Figure 11 shows the interface profiles for a drop in a uniaxial extensional flow according to the numerical results from the viscous potential flow theory, with density ratio $\Lambda = 0.8$, viscosity ratios $\beta = 0.1$ and $\beta = 1$, Reynolds numbers $Re = 20$ and $Re = 200$ and Weber number $We = 3$. We have chosen these values of Weber and Reynolds numbers because they are in the same order as those used for the bubble. In particular, $Re = 20$ should correspond to a regime in which both inertia and viscosity affect the flow dynamics. First, one notices that, as in the inviscid case for the drop, the break-up is tertiary. Comparing cases (*a*) and (*b*) for $Re = 200$ and cases (*c*) and (*d*) for $Re = 20$ indicates that increasing the viscosity ratio from $\beta = 0.1$ to 1 increases the break-up time, a result that can be anticipated because of the resistance that a more viscous liquid offers to motion. In addition, for a fixed β, decreasing Re, e.g. increasing the viscous effects in the flow, leads to higher break-up times and much more elongated drops; in particular, the length of the intermediate satellite drop considerably increases and the size of the daughter drops on the sides, which are large for $Re = 200$, diminishes. A comparison between cases (*a*) and (*b*) reveals that for $Re = 200$ changing β from 0.1 to 1 is of little consequence for the drop morphology, whereas for $Re = 20$ the final length of the drop increases in a rather noticeable amount, although the overall shapes are similar.

Contrasting with the inviscid case of figure 17(*a*) of appendix B, adding the viscous effects of the irrotational motion for $Re = 200$ in figure 11(*a*,*b*), yields a stretching of the axial drop dimension and, in particular, the intermediate satellite drop stretches about 26 % at the time of break-up. Surprisingly, for $Re = 200$, cases (*a*) and (*b*), the drops break-up in a shorter time than for the inviscid case ($t_b = 7.425$). This is in contrast to the bubble case in which the break-up time for the inviscid system

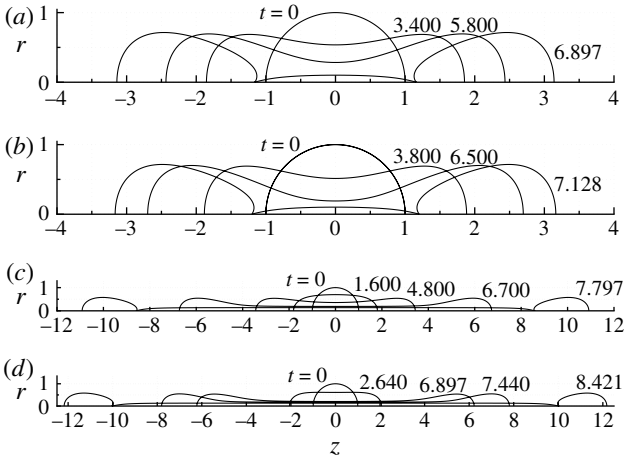

FIGURE 11. Deformation of a drop in a uniaxial straining flow from a viscous potential flow analysis with density ratio $\Lambda = 0.8$, Weber number $We = 3.0$ and (*a*) $\beta = 0.1$ and $Re = 200$, (*b*) $\beta = 1.0$ and $Re = 200$, (*c*) $\beta = 0.1$ and $Re = 20$ and (*d*) $\beta = 1.0$ and $Re = 20$.

is a lower bound for the viscous system (see figure 8). Performing computations with $Re > 200$, for $We = 30$ and $\Lambda = 0.8$ (not shown here), we obtained break-up times increasing with Re towards the inviscid limit. This result, that the break-up time is shorter than the time for the inviscid case for $Re = 200$ whereas it is longer for $Re = 20$, perhaps has to do with the unequal distribution of the liquid in the drop: for $Re = 200$, it mostly occupies two big lateral drops each of them having similar axial length as the slender satellite drop bridging them. On the other hand, for $Re = 20$, cases (*c*) and (*d*), the drops attain large elongations of about four times those attained in the case of $Re = 200$, hence the process of deformation takes longer before pinch-off in comparison with the inviscid case of figure 17(*a*) and the viscous case of $Re = 200$. Finally, the volume changes in the drop during the entire deformation resulting from the numerical solutions are within 0.07 % for all of the cases presented in figure 11.

As discussed by RDZ for the inviscid case, extremely elongated drops, such as those depicted in figure 11(*c*,*d*) for $Re = 20$, become of the same size as the eddy that tends to break them up and, therefore, the axisymmetric configuration is not preserved as the ligament is bent by the action of the background flow and the model assumed in this work no longer holds on quantitative terms. However, some relevant features of the drop shape are still reproduced, i.e. the drop length and tertiary break-up pattern.

As a reference, for the bubble case represented in figure 9(*c*), the number of elements after the last time step was 412, whereas for the drop represented in figure 11(*c*) this number was 1248. The initial number of elements in both cases was 128. The number of Runge–Kutta steps for the bubble was about 39 000; for the drop this number was 2.5 times that for the bubble. The code execution time for the drop in this particular case was about 50 times that for the bubble.

The evolution of the drop minimum neck radius r_{min} with time t and time to pinch-off $\tau = t_b - t$ when the interface approaches pinch-off is plotted in figures 12 and 13, respectively, for $We = 3$, $\beta = 0.1$ and two values $Re = 20$ and 200. Figures 12(*b*) and 13(*b*) show that $r_{min} \sim \tau^{2/3}$ for $Re = 200$, in agreement with the inviscid potential regime (Leppinen & Lister 2003), as expected for such a large value of the

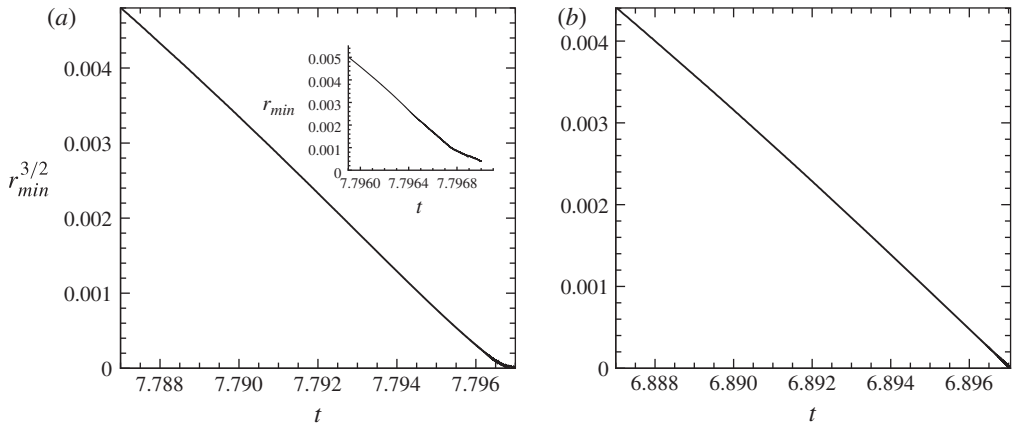

FIGURE 12. Power of the minimum neck radius $r_{min}^{3/2}$ as a function of time t approaching pinch-off for a viscous drop within another viscous liquid with density ratio $\Lambda = 0.8$, Weber number $We = 3$, viscosity ratio $\beta = 0.1$ and Reynolds number (*a*) $Re = 20$ and (*b*) $Re = 200$. The figures show that the minimum neck radius approaches pinch-off following the scaling $r_{min} \sim \tau^{2/3}$ as the time to pinch-off $\tau = t_b - t \to 0$. In figure (*a*) a change to the scaling $r_{min} \sim \tau$ occurs when rupture is imminent.

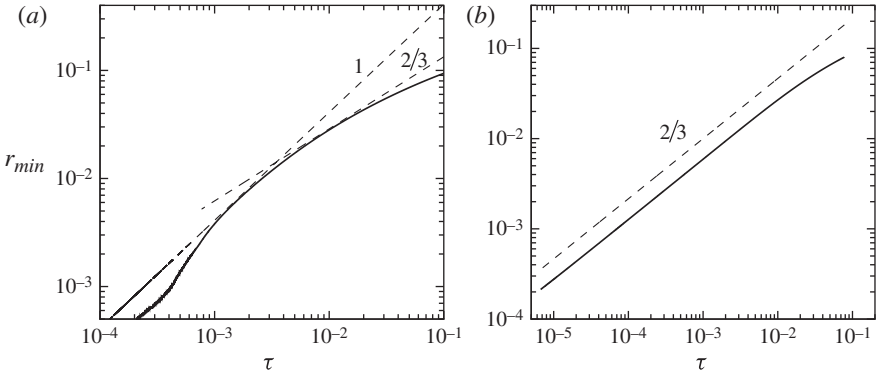

FIGURE 13. Minimum neck radius r_{min} as a function of the time to break-up $\tau = t_b - t$ for a viscous drop within another viscous liquid with density ratio $\Lambda = 0.8$, Weber number $We = 3$, viscosity ratio $\beta = 0.1$ and Reynolds number (*a*) $Re = 20$ and (*b*) $Re = 200$. The numerical results from the present work are given by the thick solid line. The labels next to the straight lines refer to the scaling laws $r_{min} \sim \tau^{2/3}$ and $r_{min} \sim \tau$.

Reynolds number. This scaling law is governed by inertia and surface tension. On the other hand, in figures 12(*a*) and 13(*a*), obtained for $Re = 20$, a transition is observed as $r_{min} \to 0$ and $\tau = t_b - t \to 0$ from the inviscid scaling to the scaling $r_{min} \sim \tau$. The latter has been identified in the literature with a regime where viscous effects are significant for the dynamics of the interface, as explained by Eggers (1993) for the case of a viscous drop in a passive ambient, and by Lister & Stone (1998) when the interaction with an external viscous fluid is considered. According to these figures, the transition to this regime occurs for $r_{min} \approx 5 \times 10^{-3}$–$7 \times 10^{-3}$. The inset in figure 12(*a*) shows that the change in r_{min} unexpectedly starts to deviate from the latter scaling at

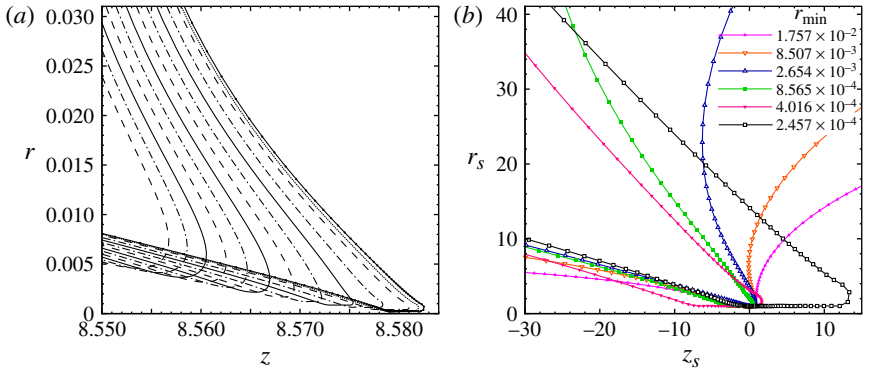

FIGURE 14. (Colour online) Interface shapes for various times approaching pinch-off for a drop of a viscous liquid in another viscous liquid computed with the viscous potential flow approach; the density ratio is $\Lambda = 0.8$, the viscosity ratio is $\beta = 0.1$, the Reynolds number is $Re = 20$ and the Weber number is $We = 3$. In figure (a) the coordinates r versus z are shown; for the last instant, the node distribution over the interface is depicted, highlighting the high density of the grid around the neck region. In figure (b) the shapes are rescaled with the minimum neck radius r_{min} and centred on z_{min}, i.e. $z_s = (z - z_{min})/r_{min}$ and $r_s = r/r_{min}$ but they do not tend to collapse and the formation of a cylindrical section is predicted. Two decades of variation of r_{min} with time are shown in the legend.

about $r_{min} \approx 1.5 \times 10^{-3}$ as $\tau \to 0$, a response that may be explained by figure 14 (see below), whereas according to figure 13(a), this deviation occurs at $r_{min} \approx 2.5 \times 10^{-3}$. This difference may be due to the magnitude of t_b (see the comment below). The break-up time t_b used to generate figure 13 is estimated from an extrapolation of the data for $r_{min} = 0$; this value is slightly higher than the final time reached in the simulations, for which $r_{min} > 0$ (this is the magnitude of t_b reported in figure 8). The trend exhibited by the curve r_{min} versus $\tau = t_b - t$ for the smallest values of r_{min} in figure 13 is influenced by the value of t_b.

In figure 14(a), we plot interface profiles for various times approaching pinch-off for $Re = 20$, $We = 3$, $\Lambda = 0.8$ and $\beta = 0.1$. We note that as $r_{min} \to 0$, the interface develops a cylindrical section whose length increases with time; this cylinder seems to start forming at about $r_{min} = 1.5 \times 10^{-3}$ in accordance with the deviation depicted in the inset of figure 12(a) and in figure 13(a). In figure 14(b), we observe that the scaled profiles r_s versus z_s do not tend to collapse as $\tau \to 0$, and hence are not self-similar with respect to this scaling, as the necking region adopts the shape of a cylindrical thread. This behaviour is in contrast with the tendencies described in figure 6 for the inviscid case, in which the interface forms cones with an apex-like necking region and the scaled coordinates evolve in a self-similar manner towards pinch-off. Experiments by Cohen *et al.* (1999) for a viscous drop dripping through another viscous liquid and simulations by Sierou & Lister (2003) for a large range of viscosity ratios have shown self-similar behaviour for the drop pinch-off; however, in their studies, the limit of no inertia (i.e. Stokes flow) is guaranteed even at macroscopic scales, and thus their conditions differ from those in our simulations. On the other hand, Doshi *et al.* (2003) conducted experiments for a water drop dripping through a very viscous liquid such that $\beta = 10^{-4}$, which is much lower than the value used here, and they observed the formation of a long thread bridging two conical sections of the drop. Another difference between the results of this work and the experiments of Cohen *et al.* (1999) and Doshi *et al.* (2003) is that in those experiments, overturning of the steep side

of the interface around the neck does not occur when the thread is formed and its slope remains lower than 90° measured from the positive z-semi-axis. In summary, we do not know whether the predicted formation of a cylindrical necking section for $\beta = 0.1$ is physically realizable or it is an artefact resulting from the lack of vorticity in our model. The results in figures 12 and 14 should be taken cautiously because the analysis of convergence carried out by increasing the initial number of elements and refinement of the spatial grid and time step did not render overlapping graphs in figure 12 but some variation was attained. Despite of this, the remarks on the scaling laws and the appearance of a transition from one scaling to the other remain valid. The position of this transition, however, varied with the simulation parameters listed above (see the comments at the end of § 4.1).

In addition, we performed simulations with $\beta = 1$ and found (not plotted here) that, after transitioning from the inviscid scaling, the linear scaling region $r_{min} \sim \tau$ persists all of the way towards the last instant considered in the simulations, for which $r_{min} = 1.8 \times 10^{-3}$; this value of r_{min} is about an order of magnitude higher than the final r_{min} for $\beta = 0.1$ (see figure 14*b*). Perhaps, continuing the computations would have revealed the formation of a cylindrical neck section; unfortunately, continuing the simulation was impractical for this case. The point of transition to the linear scaling is observed at $r_{min} \approx 8 \times 10^{-3}$ in agreement with the predictions of the theory $r_{min} \sim \beta^{-1} Oh_i^2$ (Lister & Stone 1998), obtained from scaling arguments that takes into account viscous effects of the internal and external fluids, and valid when both fluids have comparable viscosities or the internal fluid is more viscous than the external fluid. Lister & Stone showed that Stokes flow is the final regime that describes the flow in the neighbourhood of the point of drop break-up as the time to pinch-off goes to zero, provided that molecular scales are not reached first. Here, $Oh_i \equiv \mu_i / \sqrt{\rho_i \gamma a}$ is the Ohnesorge number based upon the properties of the internal fluid, which can be easily computed combining We, Re, Λ and β to eliminate parameter M. With $\beta = 1$ and the other parameters known as well ($We = 3$, $Re = 20$, $\Lambda = 0.8$), we have $Oh_i = 0.097$ and $r_{min} = 9 \times 10^{-3}$. As in the case of $\beta = 0.1$, the conclusions drawn for $\beta = 1$ may be contingent upon the values set for the simulation parameters mentioned above.

Even though data for the transient of interface deformation from the solution of the unsteady incompressible Navier–Stokes equations have not been found for the problem considered here, a comparison with data from computations of rotational flows is still possible in the case of steady shapes, since Ramaswamy & Leal (1997) obtained numerical solutions for those equations, dropping the unsteady terms, for the case of a drop in a uniaxial extensional flow for a wide range of density and viscosity ratios, varying the Weber number, and considering several values of the Reynolds number. They presented the results in terms of the deformation parameter, $D_f \equiv (l_z - l_r)/(l_z + l_r)$, where l_z and l_r are half the dimension of the drop measured on the z-axis and on the r-axis (plane $z = 0$), respectively (see figure 2); D_f is identically zero for a spherical interface. Results assuming the potential flow of viscous fluids for $\Lambda = 1$, $\beta = 1$ lead to $D_f = 0.13$ for the pair $(Re, We) = (10, 1)$, $D_f = 0.05$ for $(100, 2)$ and $D_f = 0.07$ for $(100, 2.4)$, whereas they reported $D_f = 0.16$ for $(10, 1)$, $D_f = 0.09$ for $(100, 2)$ and $D_f = 0.12$ for $(100, 2.4)$, using our notation. Therefore, although qualitatively our predictions follow the trend of their results, large quantitative differences are observed and their results are underpredicted by ours. Because a very long time period passes between start-up and the reaching of the steady state in comparison with typical break-up times in the supercritical conditions (steady state is reached in time periods about an order of magnitude longer than typical drop break-up times, roughly), the distribution of vorticity in the actual flow away from the interface where it is generated

produces strong deviations of the actual velocity field from irrotationality. In fact, for a steady interface, the fluid is at rest everywhere within the drop from the potential flow solution, whereas the external flow slips at the interface. On the other hand, when vorticity is allowed, the non-slip condition at the boundary drives the motion of the internal fluid. Based on the prediction of the deformation parameter for a steady drop, viscous potential flow turns out to be an inadequate approximation for the cases considered in this exercise.

5. Concluding remarks

The deformation of a bubble or drop in a uniaxial extensional flow starting from a spherical shape is studied in this work. The problem formulation adopted here assumes the potential flow of two viscous, incompressible fluids; hence, the effects of the vorticity are neglected in this approximation. The parameters governing the bubble or drop break-up process studied here are the ratios of internal to external fluid densities and viscosity, Λ and β, respectively, and the Reynolds and Weber numbers, Re and We, respectively, defined in terms of the external fluid properties and the principal strain rate in the far field.

Owing to the irrotational assumption, a boundary integral method for axisymmetric potential problems on both interior and exterior domains with appropriate constraints at the interface was chosen. The governing equations are solved by adopting the numerical method proposed by RDZ, who considered the same physical setup although for the flow of inviscid fluids.

We presented the comparison of the results obtained here for the bubble with results from computations involving the unsteady, incompressible Navier–Stokes equations carried out by REV using a level-set method. Such a comparison was not possible for the drop, since numerical works of this class have not been reported in the literature known to us. From the analysis of the results presented in this work, the following conclusions can be drawn. First, for the case of the *bubble* for which the density and viscosity ratios $\Lambda \ll 1$ and $\beta \ll 1$, we draw the following conclusions:

(i) For the subcritical condition, for which $We < We_c$ so that the bubble does not break up, the results from the viscous irrotational solution show good agreement with the predictions from the Navier–Stokes solver for the time variation of the bubble axial dimension and during various cycles of oscillations, not only for the largest Reynolds numbers considered, i.e. $Re = 200$, 500 and 1000, but also for $Re = 20$ and $Re = 50$, for which the amplitude of the oscillations are rapidly damped. This tendency is a consequence of the irrotational initial condition.

(ii) For the supercritical condition, for which We is such that the bubble breaks up, the viscous potential flow computations result in interface shapes evolving towards pinch-off that are very similar to the bubble shapes obtained from the solution of the Navier–Stokes equations. For a fixed Reynolds number, the break-up time decreases as the Weber number increases. For a set of intermediate and large Reynolds numbers, the break-up time computed here shows good agreement with Revuelta's predictions in the interval $3 \leqslant We \leqslant 6$. For $We > 6$ and up to the maximum value considered in this study ($We = 100$), viscous potential flow tends to underpredict the break-up time, especially for the lowest Reynolds numbers considered, namely, $Re = 20$ and $Re = 50$. For the largest Re, differences are relatively small between the irrotational and rotational theories. The predictions from the inviscid theory provide a lower bound for the break-up time, which

decreases with increasing Re for fixed We. In the interval $We_c < We < 3$, discrepancies between both theories become noteworthy.

In the case of the *drop*, which in the supercritical condition breaks up into three daughter drops, we highlight the following findings from the computations performed considering potential flow of two viscous fluids:

(i) From the evolution of the shape of a drop computed for a density ratio $\Lambda = 0.8$, a Reynolds number $Re = 200$, viscosity ratios $\beta = 0.1$ and 1 and Weber number $We = 3$, the morphology and length scales are similar to those for the inviscid case. Decreasing to $Re = 20$ renders totally different shapes: approaching pinch-off, the drop becomes very elongated and slender, with lateral daughter drops having a smaller volume than the intermediate cylindrical daughter drop. For these elongated drops with $Re = 20$, the break-up time is longer than for the $Re = 200$ case. Unexpectedly, the break-up time for $Re = 200$ was shorter than for the inviscid case, in contrast to the more viscous case of $Re = 20$.

(ii) Comparison of the deformation parameter for the steady-state shapes from viscous potential flow with those from the Navier–Stokes equations reveal large discrepancies. This may be explained by the fact that, in the actual flow, a rotational flow exists within the drop as a result of the non-slip condition, whereas in the irrotational solution, the internal fluid is at rest.

(iii) For two cases determined by $Re = 20$ and $Re = 200$, $We = 3$, $\Lambda = 0.8$ and $\beta = 0.1$, the neck minimum radius evolves with time towards pinch-off as $r_{min} \sim \tau^{2/3}$ following the inviscid scale; however, for $Re = 20$, a transition occurs to the scaling $r_{min} \sim \tau$, for which viscous effects become relevant for the interface motion. As the motion proceeds, the change in the neck radius deviates from this linear variation presumably because of the formation of a cylindrical thread. Finally, for $Re = 20$, the approach to pinch-off for rescaled interface shapes was not self-similar according to viscous potential flow when the interface coordinates are normalized with the minimum radius.

The authors gratefully acknowledge the support of the Applied Mathematics Division of the National Science Foundation under ARRA, and grant number 0302837. J.C.P. acknowledges the support of the University of Minnesota Graduate School Dissertation Fellowship, awarded for the academic year 2007–2008. Computational resources used to carry out this investigation have been provided by the Minnesota Supercomputer Institute for Advance Computational Research at the University of Minnesota. We thank D. Leppinen for his kindness in providing his code for computing quintic splines that served as basis for our own code. We also acknowledge enlightening conversations with J. M. Gordillo and J. Rodríguez-Rodríguez on their formulation for the inviscid case and numerical scheme, and with W. A. Sirignano about the problem set-up. We are indebted to the anonymous reviewers; their thoughtful comments and inquiries have improved the paper significantly. The first draft of this paper was assembled during the stay of J.C.P. at the Department of Mechanical and Aerospace Engineering of the University of California, Irvine, in the winter of 2010. This author is grateful for their support and hospitality.

Appendix A. Normal component of the strain rate and mean curvature

The notation used in (3.5) for the normal component of the viscous stress comes from standard vector differential formulae presented in terms of a local orthogonal

curvilinear coordinate system that describes the position of points on the interface and includes coordinate n_i as defined above (see Batchelor 1967, Appendix 2). With this aid, one can readily show that the normal component of the dimensionless strain rate at points on the interface can be written as

$$\boldsymbol{n}_i \cdot \nabla \otimes \nabla \phi_{(i,e)} \cdot \boldsymbol{n}_i = \frac{\partial^2 \phi_{(i,e)}}{\partial n_i^2} \tag{A 1}$$

and the two subscripts i and e are needed because this quantity, in general, is discontinuous across the interface (see below). This identity has been used in (3.5).

For an axisymmetric problem, it is convenient to introduce the set of local orthogonal curvilinear coordinates (n_i, s, ζ), where n_i and ζ have been defined above and s is the (dimensionless) arclength measured on a meridian curve Γ that results from the intersection of the surface $\mathscr{S}$ representing the interface with a plane containing the axis of symmetry (z-axis); s increases in the counterclockwise direction according to figure 2. Because $\partial(\ )/\partial\zeta = 0$, and using Laplace's equations for the potentials $\phi_{(i,e)}$ written in terms of these curvilinear coordinates, one can show that

$$\boldsymbol{n}_i \cdot \nabla \otimes \nabla \phi \cdot \boldsymbol{n}_i = \frac{\partial^2 \phi}{\partial n_i^2} = -\frac{\partial^2 \phi}{\partial s^2} + 2\kappa \frac{\partial \phi}{\partial n_i} - \frac{1}{r}\frac{\partial r}{\partial s}\frac{\partial \phi}{\partial s} \quad \text{for } r > 0 \text{ and} \tag{A 2a}$$

$$\boldsymbol{n}_i \cdot \nabla \otimes \nabla \phi \cdot \boldsymbol{n}_i = \frac{\partial^2 \phi}{\partial n_i^2} = -2\frac{\partial^2 \phi}{\partial s^2} + 2\kappa \frac{\partial \phi}{\partial n_i} \quad \text{for } r = 0, \tag{A 2b}$$

where κ denotes the mean curvature of the interface (see below). For simplicity, ϕ is written in (A 2) without subscripts (i, e). Note that even though $\partial\phi/\partial n_i$ is continuous across the interface by condition (3.4), the second derivatives $\partial^2\phi_i/\partial n_i^2 \neq \partial^2\phi_e/\partial n_i^2$, in general, because tangential derivatives $\partial\phi/\partial s$ and $\partial^2\phi/\partial s^2$ are discontinuous as a consequence of the jump in potential ϕ.

Regarding the surface tension term in the right-hand side of (3.5), by using the set of orthogonal coordinates (n_i, s, ζ), we have

$$-\nabla_{\parallel} \cdot \boldsymbol{n}_i = 2\kappa = -\frac{\partial z}{\partial s}\frac{\partial^2 r}{\partial s^2} + \frac{\partial r}{\partial s}\frac{\partial^2 z}{\partial s^2} + \frac{1}{r}\frac{\partial z}{\partial s} \quad \text{for } r > 0 \quad \text{and} \tag{A 3a}$$

$$-\nabla_{\parallel} \cdot \boldsymbol{n}_i = 2\kappa = 2\frac{\partial^2 z}{\partial s^2} \quad \text{for } r = 0, \tag{A 3b}$$

where the latter expression is obtained by recognizing that $\partial z/\partial s = 0$ and $\partial r/\partial s = 1$ at $r = 0$. Similar expressions to those in (A 2) and (A 3) have been presented by Georgescu *et al.* (2002).

Appendix B. Additional validation steps

Results for the time evolution of a bubble or drop in a uniaxial straining flow from boundary integrals simulations by RDZ considering inviscid fluids are used to further validate our code in the case of large deformations. They considered that initially the interface is spherical. If the viscosity is set to zero, the parameters controlling the dynamics are the Weber number and the density ratio. Their results indicate that above a certain critical value of *We*, the bubble breaks up, whereas for values of *We* below that threshold, the bubble undergoes large oscillations without breaking up. For the purpose of comparison, we have chosen some of the cases considered by RDZ. First, we consider a bubble with density ratio $\Lambda = 0.0012$ and Weber numbers $We = 1.0$, 2.19, 10.0 and $We \to \infty$; the first two values correspond to subcritical conditions

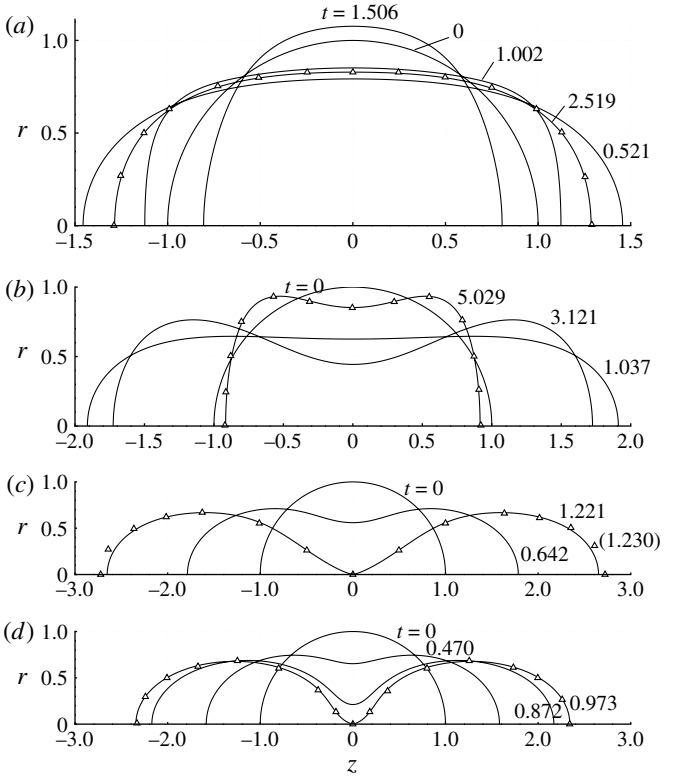

FIGURE 15. Deformation of a bubble in a uniaxial straining flow from an inviscid potential flow analysis with density ratio $\Lambda = 0.0012$ and different Weber numbers: (*a*) $We = 1.0$, (*b*) $We = 2.19$, (*c*) $We = 10.0$ and (*d*) $We \to \infty$. The solid lines represent the results from the present work and the Δ denotes results from RDZ. This comparison is part of the validation stage of the computational code developed in this work.

and the last two cases result in break-up. RDZ have found a critical Weber number $We_c = 2.3$. Figure 15 shows our numerical simulations using the numerical method presented in § 3.2 for various times. For the final time in each case, the predictions by RDZ are shown with symbols and the agreement is excellent. It should also be mentioned that the final time t_b from our simulations agree very well with their final time. The largest difference is for case (*c*), for which our $t_b = 1.221$ and theirs $t_b = 1.230$; this amounts to a discrepancy of $-0.7\,\%$ that we consider insignificant. Since the fluids are incompressible, the volume of the bubble or drop must remain constant; by numerical integration of a body of revolution around the z-axis, this volume has been computed after every time step and errors within $0.02\,\%$ where obtained for the four cases shown in figure 15. This demonstrates the mass preserving attribute of the numerical scheme used in this work. As a reference, with 129 nodes, the relative error (%) in the computation of the volume for the initial sphere is about 2×10^{-12}.

The results shown in figure 15 were computed using 128 elements, with node staggering and grid refinement. Owing to the latter feature, the number of elements increased with time leading to a number of elements in the order of 350 at the last instant of the computations. Test computations with double the initial number of

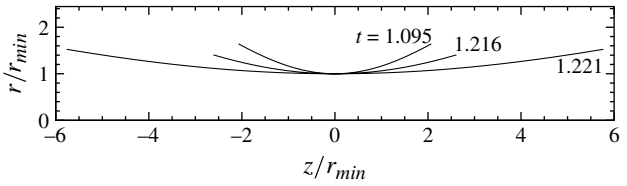

FIGURE 16. Normalized bubble profile approaching pinch-off for a Weber number $We = 10.0$, density ratio $\Lambda = 0.0012$ and inviscid fluids. Here, r_{min} denotes the minimum radius of the bubble neck. The various curves are very well fitted by the parabolic profile $z/r_{min} = 1 + ar^2/r_{min}^2$, where $r_{min} = 0.220$ and $a = 0.152$ for $t = 1.095$; $r_{min} = 0.035$ and $a = 0.060$ for $t = 1.216$ and $r_{min} = 0.002$ and $a = 0.016$ for $t = 1.221$.

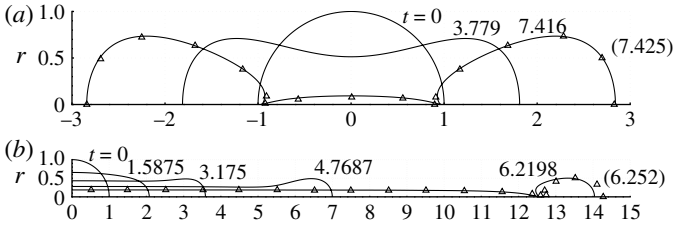

FIGURE 17. Deformation of a drop in a uniaxial straining flow from an inviscid potential flow analysis with density ratio $\Lambda = 0.8$ and Weber numbers (*a*) $We = 3.0$ and (*b*) $We = 10$. The solid lines represent the results from the present work and the Δ denotes results from RDZ. This comparison is part of the validation stage of the computational code developed in this work.

elements lead to the same profiles as those shown here. In addition, using a maximum allowable time step of 10^{-5} (recall that we are using an adaptive time stepping) instead of our standard maximum of 10^{-4} did not render significant changes either. Similar tests were also conducted for a few of the cases reported here for the inviscid drop as well as for the calculations concerning the irrotational motion of viscous fluids, and the results for the overall interface shape and break-up time show insignificant variation with both the increment of the number of elements at start-up and the reduction of the maximum time step size.

Owing to the symmetry imposed by the initial and boundary conditions, the deformed interface shows reflectional symmetry and the minimum radius is attained at the equatorial plane when the necking region develops in the cases considered here for the bubble. If the coordinates of the interface are normalized by the minimum radius r_{min} (figure 16), the normalized profile becomes slender as time progresses, since the length scale in the radial direction decreases faster than the scale along the axial direction, as reported by Gordillo *et al.* (2005). A parabolic function fits these curves very well.

Figure 17 depicts the time evolution of the interface for an inviscid drop within an inviscid fluid with a density ratio $\Lambda = 0.8$ and two different Weber numbers. In contrast to the case of a bubble where break-up has been observed to be binary in experiments, for the case of a drop the tertiary break-up has been reported (see § 1). This is reproduced by the simulations. For the smallest $We = 3$, the slender satellite drop and the two large droplets on the sides have similar axial length scales. On the other hand, for the largest $We = 10$ considered, a central elongated ligament is formed

with axial length of about 12 times the initial drop length, and break-up occurs near the ends of the slender drop. Also, break-up times attained for the drop are larger than in the case of the bubble. Comparison of the shapes predicted by our code with those by RDZ (symbols) for $We = 3$ demonstrate very good agreement, which is also obtained for the break-up time. For $We = 10$, the drop shape predicted by the present code is similar to that by RDZ; however, discrepancies arise in the neck region (pinch-off area) and in the shape of the daughter drops at the tips. This is because we implemented grid refinement in our simulations, whereas RDZ did not. Indeed, when we disable grid refinement and enforce equally spaced nodes, our result with 513 nodes (not shown) and that by RDZ coincide in shape. We also highlight that volume is preserved in the simulations for the drop up to the final time within 0.09 %, even in the case where the axial length scale changes so dramatically (e.g. $We = 10$).

REFERENCES

ABRAMOWITZ, M. & STEGUN, I. A. (eds.) 1964 *Handbook of Mathematical Functions with Formulas, Graphs, and Mathematical Tables*. US Department of Commerce, tenth printing, December 1972.

ANDERSSON, R. & ANDERSSON, B. 2006 On the breakup of fluid particles in turbulent flows. *AIChE J.* **52**, 2020–2030.

BATCHELOR, G. K. 1967 *An Introduction to Fluid Dynamics*. Cambridge University Press.

BOLANOS-JIMÉNEZ, R., SEVILLA, A., MARTÍNEZ-BAZÁN, C., VAN DER MEER, D. & GORDILLO, J. M. 2009 The effect of liquid viscosity on bubble pinch-off. *Phys. Rev. Lett.* **21**, 072103.

BURTON, J. C., WALDREP, R. & TABOREK, P. 2005 Scaling and instabilities in bubble pinch-off. *Phys. Rev. Lett.* **94**, 184502.

CANOT, E., DAVOUST, L., HAMMOUMI, M. E. & LACHKAR, D. 2003 Numerical simulation of the buoyancy-driven bouncing of a 2-D bubble at a horizontal wall. *Theor. Comput. Fluid Dyn.* **17**, 51–72.

CHEN, Y. J. & STEEN, P. H. 1997 Dynamics of inviscid capillary breakup: collapse and pinchoff of a film bridge. *J. Fluid Mech.* **341**, 245–267.

COHEN, I., BRENNER, M. P., EGGERS, J. & NAGEL, S. R. 1999 Two fluid drop snap-off problem: experiments and theory. *Phys. Rev. Lett.* **83**, 1147–1150.

DAY, R. F., HINCH, E. J. & LISTER, J. R. 1998 Self-similar capillary pinchoff of an inviscid fluid. *Phys. Rev. Lett.* **80**, 704–707.

DOSHI, P., COHEN, I., ZHANG, W. W., SIEGEL, M., HOWELL, P., BASARAN, O. A. & NAGEL, S. R. 2003 Persistence of memory in drop breakup: the breakdown of universality. *Science* **302**, 1185–1188.

EASTWOOD, C. D., ARMI, L. & LASHERAS, J. C. 2004 The breakup of immiscible fluids in turbulent flows. *J. Fluid Mech.* **502**, 309–333.

EGGERS, J. 1993 Universal pinching of 3D axisymmetric free-surface flows. *Phys. Rev. Lett.* **71**, 3458–3460.

GEORGESCU, S. C., ACHARD, J. L. & CANOT, E. 2002 Jet drops ejection in bursting gas bubbles processes. *Eur. J. Mech. (*B/*Fluids*) **21**, 265–280.

GORDILLO, J. M. 2008 Axisymmetric bubble collapse in a quiescent liquid pool. I. Theory and numerical simulations. *Phys. Fluids* **20**, 112103.

GORDILLO, J. M., SEVILLA, A., RODRÍGUEZ-RODRÍGUEZ, J. & MARTÍNEZ-BAZÁN, C. 2005 Axisymmetric bubble pinch-off at high Reynolds numbers. *Phys. Rev. Lett.* **95**, 194501.

GUIDO, S. & GRECO, F. 2004 Dynamics of a liquid drop in a flowing immiscible liquid. In *Rheology Reviews 2004* (ed. D. M. Binding & K. Walters), pp. 99–142. The British Society of Rheology.

HEISTER, S. D. 1997 Boundary element methods for two-fluid free surface flows. *Engng Anal. Bound. Elem.* **19**, 309–317.

HILBING, J. H., HEISTER, S. D. & SPANGLER, C. A. 1995 A boundary-element method for atomization of a finite liquid jet. *Atomiz. Sprays* **5**, 621–638.

HINZE, J. O. 1955 Fundamentals of the hydrodynamics mechanism of splitting in dispersion processes. *AIChE J.* **1**, 289–295.

JOSEPH, D. D., FUNADA, T. & WANG, J. 2007 *Potential Flows of Viscous and Viscoelastic Fluids*. Cambridge University Press.

JOSEPH, D. D. & RENARDY, Y. Y. 1993 *Fundamentals of Two-Fluid Dynamics, Part I: Mathematical Theory and Applications*. Springer.

KANG, I. S. & LEAL, L. G. 1987 Numerical solution of axisymmetric, unsteady free boundary problems at finite Reynolds number. I. Finite-difference scheme and its application to the deformation of a bubble in a uniaxial straining flow. *Phys. Fluids* **30**, 1929–1940.

KANG, I. S. & LEAL, L. G. 1990 Bubble dynamics in time-periodic straining flows. *J. Fluid Mech.* **218**, 41–69.

KEIM, N. C., MØLLER, P., ZHANG, W. W. & NAGEL, S. R. 2006 Breakup of air bubbles in water: memory and breakdown of cylindrical symmetry. *Phys. Rev. Lett.* **97**, 144503.

KELLER, J. B. & MIKSIS, M. J. 1983 Surface tension driven flows. *SIAM J. Appl. Maths* **43**, 268–277.

KOLMOGOROV, A. N. 1949 On the breakage of drops in a turbulent flow. *Dokl. Akad. Nauk SSSR* **66**, 825–828.

LAMB, H. 1932 *Hydrodynamics*, 6th edn. Cambridge University Press, reprinted by Cambridge University Press, 1993.

LEPPINEN, D. & LISTER, J. R. 2003 Capillary pinch-off in inviscid fluids. *Phys. Fluids* **15**, 568–578.

LISTER, J. R. & STONE, H. 1998 Capillary breakup of a viscous thread surrounded by another viscous fluid. *Phys. Fluids* **10**, 2758–2764.

LONGUET-HIGGINS, M. S. & COKELET, E. D. 1976 The deformation of steep surface waves on water. I. A numerical method of computation. *Proc. R. Soc. Lond. Ser.* A **350**, 1–26.

LUNDGREN, T. S. & MANSOUR, N. N. 1988 Oscillations of drops in zero gravity with weak viscous effects. *J. Fluid Mech.* **194**, 479–510.

MARTÍNEZ-BAZÁN, C., MONTANES, J. L. & LASHERAS, J. C. 1999*a* On the breakup of an air bubble injected into a fully developed turbulent flow. Part 1. Breakup frequency. *J. Fluid Mech.* **401**, 157–182.

MARTÍNEZ-BAZÁN, C., MONTANES, J. L. & LASHERAS, J. C. 1999*b* On the breakup of an air bubble injected into a fully developed turbulent flow. Part 2. Size pdf of the resulting daughter bubbles. *J. Fluid Mech.* **401**, 183–207.

MELVILLE, W. K. 1996 The role of surface-wave breaking in air–sea interaction. *Annu. Rev. Fluid Mech.* **18**, 279–321.

MIKSIS, M., VANDEN-BROECK, J.-M. & KELLER, J. B. 1982 Rising bubbles. *Phys. Fluids* **123**, 31–41.

OGUZ, H. & PROSPERETTI, A. 1990 Bubble entrainment by the impact of drops on liquid surfaces. *J. Fluid Mech.* **219**, 143–179.

PADRINO, J. C. 2010 Topics in viscous potential flow of two-phase systems. Chapter 2: Viscous irrotational analysis of the deformation and break-up time of a bubble or drop in uniaxial straining flow. PhD thesis, University of Minnesota, Minneapolis, MN, USA.

PADRINO, J. C., FUNADA, T. & JOSEPH, D. D. 2008 Purely irrotational theories for the viscous effects on the oscillations of drops and bubbles. *Intl J. Multiphase Flow* **34**, 61–75.

QUAN, S. & HUA, J. 2008 Numerical studies of bubble necking in viscous liquids. *Phys. Rev. Lett.* **77**, 066303.

RAMASWAMY, S. & LEAL, L. G. 1997 A note on inertial effects in the deformation of Newtonian drops in a uniaxial extensional flow. *Intl J. Multiphase Flow* **23**, 561–574.

REVUELTA, A., RODRÍGUEZ-RODRÍGUEZ, J. & MARTÍNEZ-BAZÁN, C. 2006 Bubble break-up in a straining flow at finite Reynolds numbers. *J. Fluid Mech.* **551**, 175–184.

RISSO, F. & FABRE, J. 1998 Oscillations and breakup of a bubble immersed in a turbulent field. *J. Fluid Mech.* **372**, 323–355.

RODRÍGUEZ-RODRÍGUEZ, J. 2004 Estudio de la rotura de gotas y burbujas en flujos a altos números de Reynolds. PhD thesis, Universidad Carlos III de Madrid, Madrid.

RODRÍGUEZ-RODRÍGUEZ, J., GORDILLO, J. M. & MARTÍNEZ-BAZÁN, C. 2006 Breakup time and morphology of drops and bubbles in a high-Reynolds-number flow. *J. Fluid Mech.* **548**, 69–86.

RODRÍGUEZ-RODRÍGUEZ, J., MARTÍNEZ-BAZÁN, C. & MONTANES, J. L. 2003 A novel particle tracking and break-up detection algorithm: application to the turbulent break-up of bubbles. *Meas. Sci. Technol.* **14**, 1328–1340.

SIEROU, A. & LISTER, J. R. 2003 Self-similar solutions for viscous capillary pinch-off. *J. Fluid Mech.* **497**, 381–403.

STROUD, A. H. & SECREST, A. H. 1966 *Gaussian Quadrature Formulae*. Prentice Hall.

THORODDSEN, S. T., ETOH, T. G. & TAKEHARA, K. 2007 Experiments on bubble pinch-off. *Phys. Fluids* **19**, 042101.